KRAS inhibition activates an actionable CD24 'don't eat me' signal in pancreas cancer

Yongkun Wei[1], Minghui Liu[1*], Er-Yen Yen[2,9*], Jun Yao[1*], Phuoc T Nguyen[1,9], Xiaofei Wang[3], Zecheng Yang[3,9], Abdelrahman Yousef[4], Dean Pan[1], Yanqing Jin[1], Madelaine S. Theady[3,9], Jungho Park[3,9], Yiming Cai[1,9], Mitsunobu Takeda[3], Matthew Vasquez[5], Yong Zhou[6,9], Hong Zhao[5], Andrea Viale[2,9], Huamin Wang[7], Dan Zhao[4], Ronald A., DePinho[8,9], Wantong Yao[3,9#], Haoqiang Ying[1,9#]

[1]Department of Molecular and Cellular Oncology, The University of Texas MD Anderson Cancer Center, Houston, TX, USA.

[2]Department of Genomic Medicine, The University of Texas MD Anderson Cancer Center, Houston, TX, USA.

[3]Department of Translational Molecular Pathology, The University of Texas MD Anderson Cancer Center, Houston, TX, USA.

[4]Department of Gastrointestinal Medical Oncology, The University of Texas MD Anderson Cancer Center, Houston, TX, USA.

[5]Systems Medicine and Bioengineering Department, Houston Methodist Cancer Center, Houston, TX, USA.

[6]Department of Integrative Biology and Pharmacology, University of Texas Health Science Center at Houston, McGovern Medical School, Houston, TX, USA.

[7]Department of Pathology, The University of Texas MD Anderson Cancer Center, Houston, TX, USA.

[8]Department of Cancer Biology, The University of Texas MD Anderson Cancer Center, Houston, TX, USA.

[9]Graduate School of Biomedical Sciences, The University of Texas MD Anderson Cancer Center and University of Texas Health Science Center, Houston, TX, USA.

*These authors contribute equally

[#] Co-corresponding authors

Author's Disclosures: R.A. DePinho is Founder and Advisor of Tvardi Therapeutics, Asylia Therapeutics, Stellanova Therapeutics, Nirogy Therapeutics, and Sporos Bioventures. No disclosures were reported by the other authors.

Abstract

$KRAS^{G12C}$ inhibitor (G12Ci) has produced encouraging, albeit modest and transient, clinical benefit in pancreatic ductal adenocarcinoma (PDAC). Identifying and targeting resistance mechanisms to G12Ci treatment is therefore crucial. To better understand the tumor biology of the $KRAS^{G12C}$ allele and possible bypass mechanisms, we developed a novel autochthonous $KRAS^{G12C}$-driven PDAC model. Compared to the classical $KRAS^{G12D}$ PDAC model, the G12C model exhibit slower tumor growth, yet similar histopathological and molecular features. Aligned with clinical experience, G12Ci treatment of $KRAS^{G12C}$ tumors produced modest impact despite stimulating a 'hot' tumor immune microenvironment. Immunoprofiling revealed that CD24, a 'do-not-eat-me' signal, is significantly upregulated on cancer cells upon G12Ci treatment. Blocking CD24 enhanced macrophage phagocytosis of cancer cells and significantly sensitized tumors to G12Ci treatment. Similar findings were observed in $KRAS^{G12D}$-driven PDAC. Our study reveals common and distinct oncogenic KRAS allele-specific biology and identifies a clinically actionable adaptive mechanism that may improve the efficacy of oncogenic KRAS inhibitor therapy in PDAC.

Significance:

Lack of faithful preclinical models limits the exploration of resistance mechanisms to $KRAS^{G12C}$ inhibitor in PDAC. We generated an autochthonous $KRAS^{G12C}$-driven PDAC model, which revealed allele-specific biology of the $KRAS^{G12C}$ during PDAC development. We identified CD24 as an actionable adaptive mechanisms in cancer cells induced upon $KRAS^{G12C}$ inhibition and blocking CD24 sensitizes PDAC to KRAS inhibitors in preclinical models.

Introduction

KRAS is the most frequently mutated oncogene in human cancer with hot-spot mutations at Glycine^{12}, Glycine^{13} and Glutamine^{61} (1). While all oncogenic KRAS mutations result in the constitutive activation of KRAS protein, different alleles exhibit somewhat distinctive biochemical properties and tissue-specific distribution patterns (2,3). Oncogenic mutations in KRAS are present in the vast majority of pancreatic ductal adenocarcinoma (PDAC) with G12D (41%), G12V (34%) and G12R (16%) being the most frequent mutations, along with other less common mutations such as Q61H (4%) and G12C (1.5%) (4,5). Retrospective analysis suggests that, among the KRAS mutations commonly found in PDAC, the G12D mutation is associated with worst prognosis (6) which mirrors survival data in lung and colon cancer patients (2), suggesting allele-specific differences in the tumor biological impact of various oncogenic KRAS alleles. It should be noted that the preclinical studies used to establish the critical function of KRAS oncogene for PDAC initiation and maintenance have been based largely on models driven by either Kras^{G12D} or Kras^{G12V} (7-12). Together, these data emphasize the need for the study of oncogenic KRAS allele-specific biology in PDAC and other cancer types.

KRAS, long considered an undruggable target, has been targeted by drugs including a KRAS^{G12C} inhibitor (G12Ci) which is approved for the treatment of KRAS^{G12C}-mutant non-small cell lung cancer (NSCLC) (13,14). In a phase II trial for KRAS^{G12C}-mutated PDAC, AMG 510 (Sotorasib) showed promising anticancer activity, with a 21% response rate and over 70% patients showing some tumor shrinkage (15). Recently, a novel KRAS^{G12D} inhibitor, MTXT1133, showed strong efficacy in pre-clinical animal models (16,17). Although While various KRAS inhibitors have transformed the treatment landscape of KRAS-driven cancers, the rapid re-emergence of tumors has severely limited their clinical benefit (18,19). Multiple studies have elucidated potential

resistance mechanisms to G12Ci in NSCLC including accumulation of additional mutations in the $KRAS^{G12C}$ oncogene, re-activation of the KRAS signaling through the hyperactivation of multiple receptor tyrosine kinases (RTKs), and cell state transformation through epithelial to mesenchymal transition (EMT) (14,20-26). However, the molecular mechanisms underlying the resistance to G12Ci in PDAC remain poorly understood, owing in part to the lack of relevant $KRAS^{G12C}$-driven preclinical models. With respect to PDAC models, the $KRAS^{G12D}$ model has proven capable of anticipating resistance mechanisms involving cancer cell instrinsic and paracrine mechanisms (27-29). Here, we have engineered a G12C PDAC model revealing a less aggressive tumor phenotype relative to the $KRAS^{G12D}$-driven model and a novel bypass mechansism in the face of AMG 510 treatment. Co-targeting CD24, a 'do not eat me' signal (30) upregulated in AMG 510-treated cancer cells, sensitizes PDAC to KRAS inhibitors, informing a highly effective co-extinction hypothesis for PDAC patients.

Results

Pancreatic-specific expression of $Kras^{G12D}$ from the endogenous allele results in the development of premalignant lesions, such as PanINs and acinar-to-ductal metaplasia (ADM), with the occasional progression to invasive carcinoma at low penetrance after a long latency period (10). Deletion or mutation of additional tumor repressors such as *Ink4a* or *Trp53* cooperates with *Kras* oncogene to accelerate the tumor progression and leads to the development of invasive PDAC at full penetrance (7,11,31). Knock-in of $Kras^{G12C}$ into mouse pancreas also induces the formation of premalignant lesions (32). To ensure full malignant progression and assess the role of $Kras^{G12C}$ in advanced PDAC and therapy response, we established a mouse model engineered with the $LSL\text{-}Kras^{G12C}$, conditional *p53* knockout ($p53^{L}$), and pancreatic-specific *p48-Cre* alleles

(32-34). The resulting *p48-Cre LSL-Kras*^{G12C} *p53*$^{L/+}$ ($K^{C}PC$) mice exhibit decreased number and area of PanIN/ADM lesions compared to age-matched $Kras^{G12D}$-driven controls (*p48-Cre LSL-Kras*^{G12D} *p53*$^{L/+}$, $K^{D}PC$) at 8, 12 and 16 weeks (Fig.1A-C). The decreased neoplastic activity of *Kras*^{G12C} aligns with decreased downstream signaling (phospho-ERK) and cell proliferation (Ki67) in premalignant epithelial cells (Fig.1D-G), suggesting that $KRAS^{G12C}$ is a less potent oncogenic allele compared to $KRAS^{G12D}$.

To gain insight into the molecular differences between theses alleles, whole transcriptomic analysis using the GeoMx Digital Spatial Profiler (DSP) platform was conducted on pan-cytokeratin+ (panCK+) epithelial cells from a total of 73 morphologically similar premalignant lesions randomly selected from the pancreatic tissues of 16-week old $K^{C}PC$ (33 lesions from 2 mice) and $K^{D}PC$ (40 lesions from 2 mice) mice (Supplementary Fig. S1A). As shown in Fig.1H, principle component analysis of the RNA-seq data indicates that, while there is limited heterogeneity between individuals within the same genotype, the molecular features of the preneoplstic lesions from the $K^{C}PC$ model can be distinguished from $K^{D}PC$ lesions, implicating KRAS allele-specific molecular underpinnings in processes of PDAC initiation. Gene Set Enrichment Analysis (GSEA) indicates enrichment of acinar cell features in G12C lesions accompanied with the significant upregulation of multiple acinar-specific genes compared to G12D lesions (Fig.1I, J; Supplementary Fig.S1B). On the other hand, G12D lesions show significant upregulation of markers of exocrine progenitor cells (Fig.1I, K; Supplementary Fig.S1C), including DCLK1 which has been shown to be a marker for stem-like cells in preinvasive PDAC (35). Moreover, lesions from both models exhibit similar level of ductal cell marker cytokerain-19 (CK19) (Supplementary Fig.S1D). These findings were further confirmed by immunofluorescence staining of pancreatic tissue of 16-week old $K^{C}PC$ and $K^{D}PC$ models,

showing that G12D epithelial lesions completely lose the expression of acinar marker, amylase, which is partially retained in G12C lesions, while DCLK1+ cells are more frequently observed in G12D lesions compared to $K^{C}PC$ model (Supplementary Fig.S1E-F). These data indicates that, compared to $KRAS^{G12D}$, $KRAS^{G12C}$ failed to induce complete ADM which is characterized with the transdifferentiation of acinar cells into progenitor-like ductal cells (36).

Tumor microenvironment (TME), in particular, the immune microenvironment plays important role for KRAS-driven PDAC initiation and progression (37). Multiplex immunofluorescence was conducted to catalog the pancreatic immune infiltration in 16 week-old $K^{C}PC$ and $K^{D}PC$ mice, when the pancreata contain extensive premalignant lesions, including ADM and PanINs. The dominant immune population in PDAC TME is myeloid cells, including macrophages, neutrophils, monocytes and dendritic cells (38). Indeed, myeloid cells are the majority of $CD45^{+}$ immune cells in the pancreata of both $K^{C}PC$ and $K^{D}PC$ mice (Fig.1L; Supplementary Fig. S1G). Interestingly, while G12D pancreata contain more granulocytes/neutrophils, the pancreata from $K^{C}PC$ mice exhibit increased dendritic cells (Fig.1L; Supplementary Fig. S1G). Morever, more CD4+ T cells, including immune suppressive regulatory T cells (Tregs), were observed in the pancreata from $K^{D}PC$ mice (Fig.1L; Supplementary Fig. S1G). Together, our data indicates that the delayed tumor development in the $K^{C}PC$ model, compared to $K^{D}PC$ model, is correlated with decreased KRAS signaling, incomplete ADM and alterations in the immune microenvironment.

The relatively weak tumor development in $K^{C}PC$ model results in significantly prolonged median overall survival compared to $K^{D}PC$ model (41 weeks vs 22 weeks) (Fig.2A). Retrospective analysis of a cohort of 231 PDAC patients from our institution (n=224 for $KRAS^{G12D}$, n=7 for $KRAS^{G12C}$) also indicates that the median overall survival of $KRAS^{G12C}$ mutant patients is longer than that of $KRAS^{G12D}$ patients (29 months vs 22 months), although the

difference does not reach statistical significance due to the limited number of $KRAS^{G12C}$ patients (Supplementary Fig.S2A). Histopathology analysis of advanced tumors from the $K^{C}PC$ model revealed similar histological feature of ductal adenocarcinoma compared to $K^{D}PC$ model or human PDAC (Fig.2B). Unlike the decreased KRAS signaling in the $K^{C}PC$ premalignant lesions, PDAC lesions from the $K^{C}PC$ and $K^{D}PC$ models exhibit similar KRAS signaling as measured by phosphor-ERK (Fig.2C), implicating additional mechanisms lead to the activation of $KRAS^{G12C}$ during tumor progression. Similar levels of KRAS downstream MAPK and AKT signaling are also observed in vitro using primary cultures derived from the $K^{C}PC$ and $K^{D}PC$ models (Fig.2D). Interestingly, total KRAS levels are considerably lower in $Kras^{G12C}$ lines compared to $Kras^{G12D}$ lines, although the amount of active form of KRAS is comparable between the two groups (Fig.2D; Supplementary Fig.S2B). Bulk RNA-seq was conducted to compare the transcriptomic features between $K^{C}PC$- and $K^{D}PC$-derived tumor cultures. Principle component analysis indicates that the $K^{D}PC$ lines are clustered into two groups representing the two major PDAC molecular subtypes (39), with the majority belonging to progenitor subtype and a few lines enriched with squamous subtype signatures (Fig.2E). Interestingly, the $K^{C}PC$ lines do not form separate group, but are clustered together with $K^{D}PC$ lines of the progenitor subtype (Fig.2E).

To more deeply interrogate the cancer cells and associated TME components, single cell RNA sequencing (scRNA-seq) was conducted on advanced tumors from $K^{C}PC$ (n=3) and $K^{D}PC$ (n=2) models. A recently published scRNA-seq data from the same $K^{D}PC$ model was also included for integrated analysis (40). Graph-based population delineation was performed and populations were assigned an identity based on lineage markers as shown in Fig. 2F. Integrated analysis of all cancer cells from 6 samples identified 4 major clusters (Fig.2G; Supplementary Fig.S2C). While the two major cancer cells clusters are enriched with signatures of the progenitor or squamous

subtype, respectively, we also identified a small population of highly proliferative cancer cells and a group of squamous subtype cancer cells with low expression feature (LF) (Fig.2G). Notably, while all four cancer cell clusters can be found across the 6 samples, the cancer cell composition exhibit strong inter-tumoral heterogeneity and no significant differences can be identified between the two KRAS genotypes (Fig.2H). As an important component of PDAC TME, cancer-associated fibroblasts (CAFs) comprised 2-30% of total cell populations among the 6 samples (Table S1). In addition to the myofibroblastic CAF (myCAF) cluster with high expression of *Acta2*, *Myl9* and *Tagln* (41), inflammatory CAF (iCAF) is the major component of the CAF population (Fig.2I-J; Supplementary Fig.S2D). Among the iCAF population, we further identified three subclusters, a cluster with high *Col12a1* expression, a cluster with high expression of *complement 3* (*C3*) and *complement 4* (*C4*), and a cluster with low expression feature (Fig.2I, J; Supplementary Fig.S2D). A *C3/C4*-high CAF population was also identified in human PDAC (42), although their function remains unclear. On the other hand, we did not consistently observe the antigen-presenting CAF (apCAF), likely due the limited cell numbers. Similar to previous report (41), among the CD45+ immune cells, myeloid cells, including macrophages, monocytes, dendritic cells and neutrophils, are the predominant component, ranging from 27-89% with no obvious correlation with KRAS genotypes (Table S2). Although the percentage of T cells among the total cells is higher in $K^{C}PC$ tumors compared to $K^{D}PC$ tumors (Table S1, P=0.03), proportion of T cells among CD45+ immune cells or the composition of different types of T cells does not show signficiant difference between the two gentoypes (Table S2). No correlation was identified between KRAS genotype and other immune cell types, such as B cells and DC cells, either (Table S2). Together, our data indicates that, while $KRAS^{G12C}$-driven PDAC premalignant lesions exhibit distinctive molecular features compared to

the $KRAS^{G12D}$-driven ones, there is no obvious cellular or molecular difference between the two KRAS genotypes once the tumor progresses to an advanced stage.

To evaluate the therapeutic impact of G12Ci in $K^{C}PC$ model, syngeneic xenograft tumors were established from two independent primary $K^{C}PC$-derived cultures and treated with AMG 510. While both $K^{C}PC$ lines are sensitive to AMG 510 in vitro with IC50 at nanomolar range (Supplementary Fig.S3A), AMG 510 treatment in vivo over the cause of 3 weeks failed to induce obvious tumor regression and instead produced stable or progressive disease based on the RECIST criteria (43) (Fig.3A-B). Recent studies in preclinical models demonstrated that the reprogramming of immune microenvironment, in particular the activation of cytotoxic T cells, is critical for the regression of $Kras^{G12D}$-driven tumors following MRTX1133 treatment (17,44). Therefore, Cytometry by Time of Flight (CyTOF) analysis was conducted to characterize the changes in the immune microenvironment of $K^{C}PC$-derived xenograft tumors upon AMG 510 treatment. Similar to the findings in $Kras^{G12D}$-driven PDAC models, the most dominant subset of CD45+ TME cells in the $K^{C}PC$ tumors is $CD11b^{+}Gr\text{-}1^{+}$ myeloid derived suppressive cell (MDSC) population, which decreased significantly following AMG 510 treatment (Fig.3C; Supplementary Fig.S3B). On the other hand, AMG 510 treatment leads to significant increase of $CD8^{+}$ T cells, dendritic cells (DCs) and macrophages (Fig.3C; Supplementary Fig.S3B). Additional analysis of macrophage population further revealed an increase of MHC II^{+} M1-like macrophages and concomitant decrease in $ARG1^{+}$ M2-like macrophages following AMG 510 treatment (Fig.3D; Supplementary Fig.S3C), indicating that $KRAS^{G12C}$ inhibition skews macrophages toward anti-tumor phenotype. IHC of xenograft tumors further verified the alterations in immune infiltration, showing increased $CD8^{+}$ T cells and $F4/80^{+}$ macrophages in AMG 510-treated tumors compared to vehicle-treated controls (Supplementary Fig.S3D).

Together, these data indicate that AMG 510 treatment engenders an anti-tumor immune profile, reminiscent of the changes in immune populations in $KRAS^{G12D}$-driven tumors treated with MRTX1133 (17,44). However, the lack of obvious KRAS inhibition-induced tumor regression in the $K^{C}PC$ model, in contrast to $KRAS^{G12D}$-driven models, implicates that cancer cells can sustain viability in a relatively 'hot' anti-tumor immune microenvironment.

A closer examination of the M1-like macrophages accumulated upon AMG 510 treatment identified significant upregulation of SHP2 phosphorylation (Fig.3E-F), an immune-inhibitory signaling marker(45), suggesting the suppression of macrophage function. Phagocytosis is the major way that macrophages clear cancer cells and cancer cells enabling evasion from phagocytosis via expression of CD47 and CD24 transmembrane proteins which act as anti-phagocytic "don't eat me" signals (30,46). CD47 or CD24 on cancer cells, by binding to SIRPa or Siglec-10 (Siglec-G in mouse), respectively, recruits SHP1 or SHP2, and inhibits phagocytosis of macrophages (30,46). In accordance with the increase in phospho-SHP2 level in macrophages, CyTOF analysis demonstrates that CD24 intensity is upregulated in cancer cells after AMG 510 treatment (Supplementary Fig.S3E). FACS analysis in two independent $K^{C}PC$ tumor lines further confirmed that CD24, but not CD47, is upregulated upon $KRAS^{G12C}$ inhibition (Fig. 3G; Supplementary S3F-G). QRT-PCR analysis indicates that the upregulation of CD24 after AMG 510 treatment is at transcription level (Fig.3H). To further interrogate the mechanisms underlying CD24 upregulation, kinase array analysis is conducted following AMG 510 treatment in $K^{C}PC$ cells as the immediate downstream signaling of KRAS oncogene is largely mediated by phosphorylation events. As expected, AMG 510 treatment results in the inhibition of multiple phosphorylation events, including the decrease of phosphorylation of MAPK and its downstream target c-Jun (Supplementary Fig.S3H). Intriguingly, STAT3

phosphorylation at tyrosine^{705} (Y^{705}), a marker for STAT3 activation (47), is increased in AMG 510-treated cells (Fig.3I; Supplementary S3H). Pre-treatment with STAT3 inhibitor C188-9 prevented the AMG 510-induced upregulation of CD24 (Fig. 3J-K; Supplementary S3I), indicating that STAT3 activation is required for the induction of CD24 in cancer cells upon $KRAS^{G12C}$ inhibition. $K^{C}PC$ cell and macrophage co-culture was established to further investigate whether the induction of CD24 in cancer cells indeed suppresses macrophage phagocytic function. As shown in Fig.3L, while AMG 510 treatment alone fails to affect macrophage phagocytosis, treatment of anti-CD24 monoclonal antibody (mAb) to block CD24-Siglec-G interaction increases macrophage phagocytosis which is further significantly enhanced by co-treatment with AMG 510.

To further evaluate translation relevance of targeting CD24, syngeneic xenograft models were established subcutaneously with $K^{C}PC$ lines for treatment with anti-CD24 mAb alone or in combination with AMG 510. While treatment with either AMG 510 or anti-CD24 mAb alone inhibits tumor growth, the combination further slows down the tumor growth and leads to tumor regression in some cases (Fig. 4A-B), suggesting the cooperation between co-targeting $KRAS^{G12C}$ and CD24. Moreover, the anti-tumor effect of AMG 510 and anti-CD24 mAb combination is accompanied with significant increase in macrophage phagocytosis (Fig.4C) and decrease of phospho-SHP2 (Fig.4D) in the xenograft tumors, suggesting the activation of macrophage function upon combination treatment. To further determine the requirement of macrophages for the anti-tumor effect of the combination therapy, tumor macrophages are depleted with anti-CSF1R mAb treatment in the $K^{C}PC$ xenograft models (Supplementary Fig.S4A). As shown in Fig.4E, depletion of macrophages completely reverses the tumor growth inhibition induced by the treatment of AMG 510 and anti-CD24 mAb, underscoring the essential

role of macrophage activation for the therapeutic effect of AMG 510 in combination with anti-CD24 mAb.

The most common KRAS mutation in human PDAC is $KRAS^{G12D}$ which is present in approximately one-third of PDAC patients (5). We next investigated whether CD24-mediated macrophage inhibition also occurs in $KRAS^{G12D}$-driven PDAC following KRAS inhibition. Similar to the observation from $K^{C}PC$ cells, treatment with $KRAS^{G12D}$ inhibitor, MRTX1133 (16), also significantly induces the transcription and cell surface level of CD24 in mouse $K^{D}PC$ cancer cells (Fig.4F-G). Importantly, treatment with anti-CD24 mAb further enhances the anti-tumor effect of MRTX1133 in syngeneic xenograft model of $K^{D}PC$ tumors (Fig. 4H). Moreover, anti-CD24 mAb in combination with MRTX1133 induces tumor regression in AsPC1-derived xenograft tumors in nude mice (Fig.4I). Together, our data indicates that targeting CD24 enhances macrophage phagocytosis and sensitizes KRAS-driven PDAC to KRAS targeted therapies.

Discussion

While the genetics of KRAS mutations in PDAC has been well-established(4,5), how these different oncogenic alleles exert common or distinct functions in PDAC biology is not well understood. Recent studies in preclinical models revealed that $KRAS^{G12R}$, a rare KRAS mutation uniquely enriched in PDAC, is defective in PI3K signaling and exhibit weaker oncogenesis in PDAC compared to G12D mutation (32,48), shedding light on the allele-specific biology of KRAS mutations. Here, our data indicates that, compared to $KRAS^{G12D}$, $KRAS^{G12C}$ leads to relatively weaker activation of the downstream MAPK signaling in premalignant lesions, which results in the delay in tumor progression in GEM model. Similar observations were also recently

reported in $KRAS^{G12C}$-driven lung cancer model (49). The decreased MAPK signaling downstream of $KRAS^{G12C}$ could be correlated with the unique biochemistry feature of the G12C mutation, which has been shown to maintain largely intact intrinsic GTPase activity (3). Recent study also revealed that $KRAS^{G12C}$ exhibit distinctive phospholipid binding profile compared to $KRAS^{G12D}$ (50), which may affect its localization in membrane nanodomains and thus impact the downstream signaling. In addition, inflammation has been shown to play a critical role in activation of KRAS signaling during PDAC initiation (51). Our data demonstrates that the immune environment in $KRAS^{G12C}$-induced premalignant lesions shows differences from that of $KRAS^{G12D}$ lesions, which may also contribute to the differential KRAS signaling observed in these two models. Notably, although the tumor development is delayed in the $K^{C}PC$ model compared to $K^{D}PC$ model, the advanced tumors from these models exhibit same pathology features, comparable level of MAPK signaling and similar molecular features. This implicates the involvement of additional genetic or epigenetic events for the full activation of $KRAS^{G12C}$ during tumor progression. Interestingly, recent analysis of colon and lung cancer samples revealed distinctive co-mutation patterns among different KRAS oncogenes, including the G12C mutation (52), pointing to the need for additional genomic analysis of co-mutations in PDAC with $KRAS^{G12C}$.

Emerging evidence suggests that the immune system may play a critical role in defining the response to KRAS-targeted therapy. Targeting KRAS oncogene in preclinical models of NSCLC and PDAC has been shown to reverse the suppressive immune microenvironment and activate anti-tumor immunity, which plays a critical role for the tumor regression (17,53). However, while the reprogramming of immune microenvironment is critical for the augmentation of anti-tumor effect elicited by KRAS targeted therapy, it may also negatively impact the durability of

therapy response through the accumulation of certain immune populations, especially the macrophages. Our data indicates that myeloid cells remain as the predominant immune cell population in the TME upon KRAS targeted therapy, implicating they may play major role in regulating tumor immunity. Indeed, it was recently shown that the recruitment of macrophage into the tumor microenvironment following genetic inactivation of $Kras^{G12D}$ in advanced mouse PDAC promote the survival of cancer cells and bypass of KRAS-dependence (27). Here, our data demonstrated that the anti-tumor function of macrophages in the TME is suppressed by the induction of CD24 in cancer cells following KRAS targeted therapy, undermining the therapeutic benefit of KRAS inhibitors. While more studies are needed to further dissect the macrophage-mediated regulation of innate and adaptive immunities following KRAS inhibition, such as the impact on NK and $CD8^+$ T cells, our study provides additional rationale for the co-targeting of immune microenvironment to achieve sustainable therapeutic response to KRAS inhibition in PDAC.

METHODS

Animal studies

Mice:

P48Cre, LSL-Kras^{G12D}, LSL-Kras^{G12C}, and p53^{L} mice have been described previously (10,32-34). Mice were interbred and maintained on C57BL/6 background in pathogen-free conditions. The C57BL/6 mice were purchased from Jackson Lab. NCr Nude mice were purchased from Taconic Biosciences. Studies were conducted under the protocols approved by the Institutional Animal Care and Use Committee.

Murine PDAC cell lines were derived from tumor-bearing K^{C}PC (49725, 50760) or K^{D}PC (55582) mice on a congenic C57BL/6 background. 49725(1×10^6) and 50760 (5×10^5) or 55582 (3×10^5) cells were suspended in 100 μL medium and injected subcutaneously into the right flank of C57BL/6 mice. Human PDAC cell line AsPC1 with KRAS G12D mutation (1×10^6) were injected into nude mice using same method. Tumor size was measured every 2 days using a caliper and calculated using the formula length × width^2/2. When tumor size reached 20 to 80 mm^3, mice were randomly grouped and administered treatment. For AMG 510 treatment, mice were administered 30 mg/kg AMG 510 [dissolved in 0.2% Hydroxypropyl methylcellulose + 0.1% Tween 80] by oral gavage daily until the tumor size reached limit. For CD24 antibody treatment, mice were injected intraperitoneally 100 μg of CD24 antibody (clone M1/69; #BE0360; Bio X Cell) or control rat IgG (clone LTF-2; #BE0090; Bio X Cell) twice a week. For MRTX1133 treatmet, mice were injected intraperitoneally 30 mg/kg MRTX1133(dissolved in 10% Captisol in 50 mmol/L citrate buffer pH 5.0) daily. For nude mice CD24 antibody

treatment, mice were injected intraperitoneally 100 μg of CD24 antibody (ATG-031; cat#HY-P99176; MCE) twice a week. On day 21, tumor tissue (n = 3/group) was harvested and prepared for single-cell suspension for further analysis. The remaining mice were monitored until the tumor size reached limit, then euthanized. Waterfall plots were calculated using the baseline tumor volume on day 0 compared with tumor volume at the end of the experiment. The percent change in tumor volume was calculated by ((final volume – initial volume)/initial volume) × 100.

Macrophage Depletion.

Once tumors reached an average volume of 20 to 80 mm^3, AMG 510 (30 mg/kg) and anti-CD24 was administered for 2 weeks. Macrophage depletion started 1 day before initiating AMG 510 and anti-CD24 treatment and continued every other day for the remainder of the experiment. Depleted mice received 400 μg of CSF1R (Clone AFS98) antibodies i.p., whereas control mice were given isotype control (MOPC-21; BE0083; Bio X Cell). Peripheral blood and tumor tissues were collected to confirm macrophage depletion via flow cytometry.

Real-time Quantitative PCR

Total RNA was isolated using RNeasy Mini Kit (Qiagen), and cDNA was synthesized using SuperScript™ III First-Strand Synthesis Super Mix (Thermo Fisher Scientific). qPCR reactions were performed using Fast SYBR Green Master Mix (Thermo Fisher Scientific) on BIO-RAD CFX96 Real-Time PCR system. The threshold cycle (Ct) value for each gene was normalized to the expression levels of ACTIN, and relative expression was calculated by normalizing the delta Ct value. The primer sequences (5′–3′) for the transcripts analyzed are as follows:

CD24 forward: CTTCTGGCACTGCTCCTACC

CD24 reverse: GAGAGAGAGCCAGGAGACCA

ACTIN forward: GGCTGTATTCCCCTCCATCG

ACTIN reverse: CCAGTTGGTAACAATGCCATGT

Cell Viability Assay

To determine IC_{50} values, 1 to 3 × 10^3 cancer cells were plated in a 96-well plate. Cells were treated 24 hours later with DMSO or serial dilutions of AMG 510 or MRTX1133. Cell viability was read 72 hours later using MTT. IC_{50} values were generated using GraphPad Prism (RRID:SCR_002798) version 9.1.2.

CyTOF analysis

Mouse Tumor Dissociation Kit (130-096-730, Miltenyi Biotec) and gentleMACSOcto Dissociator (130-096-427, Miltenyi Biotec) were used to digest the excised tumors from mice. Cells were then blocked with CD16/CD32 (156604; Biolegend) antibody followed by incubation with a mixture of metal-labeled antibodies (Supplementary Table S3) for 1 hour at room temperature. Cisplatin (195Pt, Fluidigm) was used as a marker to detect dead cells. Cell-ID Ir-intercalator (Fluidigm) was incubated overnight at 4°C. The samples were analyzed by using the Helios System (Fluidigm) from MD Anderson Flow Cytometry and Cellular Imaging Core Facility. Data were processed by the FlowJo (RRID:SCR_008520) software and Cytobank (RRID:SCR_014043; Cytobank, Inc.).

IHC staining

Murine tumors were fixed overnight in 10% formalin. After 24 hours, tissues were transferred to 70% ethanol and processed for paraffin embedding. Tissues were sectioned at 5 μm. For immunofluorescence staining, slides were deparaffinized and rehydrated through a series of xylene and ethanol washes. Slides underwent antigen retrieval (Antigen Retrieval Citra Plus solution, Biogenex #HK080, 95 °C for 15 min) followed by blocking with 5% goat serum and 1% BSA in PBS 0.1% Triton-X100 for 1 hour at room temperature. Primary antibodies were added to the slides and incubated overnight at 4°C. Slides were then washed 2× with PBS 0.1% Triton-X100 and incubated with secondary antibodies (Alexa Fluor secondaries, 1:150) for 1 hour at room temperature. Nuclei were counterstained with DAPI (1:1,000). Slides were mounted with ProLong Diamond Antifade Mountant and coverslipped. Images were scanned using PE Vectra Polaris. QuPath and Image J software was used for quantitation. For IHC staining, antigen retrieval was carried out by heating for 12 minutes in DAKO Target Retrieval Solution using microwave. Sections were incubated with 3% H_2O_2 for 30 min at room temperature to block endogenous peroxidase activity. After incubating in 10% normal goat or horse serum for 1 h to block non-specific binding of IgG, sections were incubated with primary antibody at 4°C overnight. After wash with PBS, sections were then incubated for 1 h with ImmPRESS-HRP polymer reagent (Vector). Samples were developed with DAB quanto chromogen substrate (Epredia) and counterstained by hematoxylin. To measure protein expression by IHC, stained sections were analyzed at ×400 resolution and scored by H-score system. An H-score (range, 0–300) was calculated as the sum of the highest intensity of staining (0, negative; 1, weak positive; 2, moderate positive; 3, strong positive) and percentage of positive cells (0%–100%; with any intensity of positive staining).

Flow Cytometry Analysis

In vitro cultured cells or single-cell suspension from mouse tumors were stained for flow cytometry analysis. Mouse Tumor Dissociation Kit (130-096-730, Miltenyi Biotec) and gentleMACSOcto Dissociator (130-096-427, Miltenyi Biotec) were used to digest the excised tumors from mice. Samples were then washed with DMEM and 10% FBS and filtered through a 70-μm strainer to obtain a single-cell suspension. Cells from mouse tissues were blocked with CD16/CD32 (156604, Biolegend). Cells were labeled with primary fluorophore-conjugated antibodies for 1 h at 4°C. Cells were washed and resuspended in flow buffer. For intracellular staining, cells were permeabilized and fixed for 30 minutes at 4°C, washed, and then stained for intracellular markers for 1 h at 4°C. Data were acquired on an BD FACSCanto II flow cytometer, with analysis performed using FlowJo (RRID:SCR_008520) version 10.9.0.

GeoMx digital spatial profiler (DSP) for RNA profiling in FFPE tissues

Five-μm FFPE tissue sections from 4 mice (2 G12C and 2 G12D) were mounted on positively charged histology slides. Slides were deparaffinized, rehydrated and incubated for 15 min in 1× Tris-EDTA pH 9.0 buffer at 100 °C. Slides were then incubated in 1 μg ml^{-1} proteinase K (Thermo Fisher Scientific, AM2546) in PBS for 15 min at 37 °C. Tissues were then fixed in 10% neutral-buffered formalin for 5 min, incubated in NBF stop buffer (0.1 M Tris Base, 0.1 M Glycine, Sigma) for 5 min twice, then washed in PBS. Tissues were then incubated overnight at 37 °C with GeoMx RNA detection probes in Buffer R (Nanostring Technologies). After washing, tissues were blocked in Buffer W (Nanostring Technologies) for 30 min at room temperature. Next, antibodies targeting PanCK and CD45 (Nanostring Technologies) in Buffer W were applied to each section for 1 h at room temperature. Slides were washed twice in fresh 2× SSC then loaded on the GeoMx Digital Spatial Profiler.

In the process entire slides were imaged at ×20 magnification and a total of 73 circular ROIs with a 200 μm diameter were selected and the GeoMx software was used to define AOIs (or segments) as one segment containing positive immunofluorescent signal for PanCK.

Once AOIs were defined, the DSP then exposed ROIs to 385 nm light (UV), releasing the indexing oligonucleotides, which were collected with a microcapillary. Indexing oligonucleotides were then deposited in a 96-well plate for subsequent processing.

Sequencing libraries were generated by PCR from the photo-released indexing oligos and AOI-specific Illumina adapter sequences, and unique i5 and i7 sample indices were added. PCR reactions were pooled and purified using AMPure XP beads (Beckman Coulter, A63881), according to the manufacturer's protocol. Pooled libraries were sequenced at 2 × 75 base pairs and with the single-index workflow on an Illumina NextSeq to generate 458 M raw reads.

PCA analysis and unsupervised clustering analysis were performed using R software (prcomp function and pheatmap package). Differential gene expression analysis was carried out using R DESeq2 package with parameters of fold change > 1.5 and adjusted p value < 0.05. GSEA analysis was performed using R fgsea package.

In vitro and in vivo phagocytosis assay

Flow cytometry-based phagocytosis assay was performed according to literature (30).

In vitro phagocytosis assays were performed by co-culture target cells and macrophages at a ratio of 100,000 target cells to 50,000 macrophages for 2 h in a humidified, 5% CO_2 incubator at 37°C in ultra-low-attachment 96-well U-bottom plates (Corning) in serum-free medium. Cells with

endogenous GFP were harvested from plates using TrypLE Express (Life Technologies) prior to co-culture. Macrophages (RAW264.7 mouse macrophage cell line) were harvested from plates using TrypLE Express. Monoclonal antibody CD24 (Clone M1/69, BioXcell) and isotype controls were added at a concentration of 10 μg/mL. After co-culture, phagocytosis assays were stopped by placing plates on ice, centrifuged at 400 g for 5 min at 4°C and stained with PE-labeled anti-F4/80 to identify mouse macrophages. Assays were analyzed by flow cytometry. Phagocytosis was measured as the number of F4/80+, GFP+ macrophages, quantified as a percentage of the total F4/80+ macrophages. Each phagocytosis reaction was performed in a minimum of technical triplicate.

For In vivo phagocytosis assay, female C57BL/6 mice, 6–8 weeks of age, were injected with 5×10^5 50760-GFP cells into the right flank. Tumors were treated with vehicle plus IgG or AMG 510 plus anti-CD24 antibody for 14 days, after which tumors were resected and dissociated mechanically and enzymatically as described above. Single-cell suspensions of tumors were blocked using anti-CD16/32 (156604, BioLegend) for 15 min on ice. Phagocytosis was measured as the percentage of PerCp-F4/80$^+$ macrophages that were also GFP$^+$.

Multiplex immunofluorescence staing

FFPE slides were deparaffinized in xylene and rehydrated in an alcohol gradient. Tissue underwent citrate-based antigen retrieval (Antigen Retrieval Citra Plus solution, Biogenex #HK080, 95 °C for 15 min) before blocking with 5% goat serum and 1% BSA in PBS 0.1% Triton-X100 for 1 h. Slides were incubated with unconjugated primary antibodies for 1 h at room temperature, followed by conjugated secondary antibodies for 1 h at room temperature, then with conjugated primary antibodies overnight at 4 °C. Slides were washed with PBS 0.1% Triton-

X100 between each step. Nuclei were counterstained with DAPI (1:1,000). Slides were mounted with ProLong Diamond Antifade Mountant and coverslipped. Images were scanned using PE Vectra Polaris. Slides were incubated with stripping buffer (62.5 mM Tris Base / Tris-HCl, 2% Sodium Dodecyl Sulfate, 0.8% Beta ME, 55°C, 30 min), and then stained with another round of antibodies. There were 4 rounds of staining and slides scan. Antibodies used were list at Supplementary Table S3. Image registration was conducted using MATLAB (The MathWorks, Inc.). Initially, the DAPI image from each imaging cycle was utilized to compute a transformation matrix using SURF features (https://doi.org/10.1016/j.cviu.2007.09.014). Subsequently, the extracted features were matched, employing the following parameters: MetricThreshold = 505, NumOctaves = 4, NumScaleLevels = 6. Automated image segmentation and quantification were performed using MATLAB (The MathWorks, Inc.). Specifically, Otsu's thresholding method and the marker-controlled watershed algorithm were applied to segment and define the nuclear regions of individual cells. Subsequently, the expression of each marker within the segmented areas was quantified based on pixel intensity. Single-cell marker expression data underwent clustering using the R implementation of Phenograph (cytofkit, https://doi.org/10.1371/journal.pcbi.1005112, 10.1088/1742-5468/2008/10/P10008) with the parameter k=15. Prior to clustering, $CD45^{+}$ $Amylase^{-}$ cells in the lesion sites are selected, and marker expression values were range normalized to the 99th percentile across all cells for each channel independently. Following clustering, the resulting clusters were labeled based on their marker expression signatures.

RNA-seq analysis

Total RNA was isolated using RNeasy Mini Kit (Qiagen). The library preparation, sample clustering and sequencing were done in MD Anderson ATGC core. The sequencing was carried out on the Illumina NovaSeq platform. Differential expression analysis of two groups in RNA-seq was performed using the DESeq2 R package. The resulting *P* value was adjusted using the Benjamini and Hochberg approach for controlling the false discovery rate. Genes with an adjusted $P < 0.05$ found by DESeq2 were assigned as differentially expressed. Gene function enrichment analysis was done with clusterProfiler by R.

Single cell RNA sequencing analysis

Tumors were dissected from mice and single-cell suspensions were obtained. Cells were counted and loaded onto the 10X device (10X Genomics). Samples were processed per the manufacturer's protocol and sequenced on an Illumina NextSeq sequencer. Single cell RNAseq raw data (fastq files) were mapped to mouse transcriptome mm10 using cellranger v7.1.0. One sample with mapped data to the same reference genome was downloaded from NCBI GEO (https://www.ncbi.nlm.nih.gov/geo/, GSE125588, sample GSM3577885). Samples were processed using R Seurat package to filter off poor quality cells based on mitochondria content and total gene numbers. Cells from all samples were merged and integrated by Seurat to remove batch effects. Cells were then clustered and annotated using cell markers from Zhang et al (54). Differential gene expression analysis was performed using R DESeq2 package with p value cutoff of 0.05 and fold change cutoff of 1.5. GSEA analysis was perfromed for activated pathways using R fgsea package using ontology annotations from MSigDB (https://www.gsea-msigdb.org/gsea/msigdb) with a p value cutoff of 2e-3.

Statistical analysis

GraphPad Prism (RRID:SCR_002798) version 9.1.2 was used for statistical analyses. Data are presented as means ± SD or SEM. Two-tailed Student *t* test and two-way ANOVA with multiple corrections were performed for comparison between groups. For IC_{50} generation, concentrations were log transformed, data were then normalized to control, and log(inhibitor) versus response (four parameters) test was used. A P value < 0.05 was considered statistically significant.

References:

1. Cox AD, Fesik SW, Kimmelman AC, Luo J, Der CJ. Drugging the undruggable RAS: Mission possible? Nat Rev Drug Discov **2014**;13:828-51
2. Haigis KM. KRAS Alleles: The Devil Is in the Detail. Trends Cancer **2017**;3:686-97
3. Hunter JC, Manandhar A, Carrasco MA, Gurbani D, Gondi S, Westover KD. Biochemical and Structural Analysis of Common Cancer-Associated KRAS Mutations. Mol Cancer Res **2015**;13:1325-35.
4. Lee JK, Sivakumar S, Schrock AB, Madison R, Fabrizio D, Gjoerup O*, et al.* Comprehensive pan-cancer genomic landscape of KRAS altered cancers and real-world outcomes in solid tumors. NPJ Precis Oncol **2022**;6:91
5. Waters AM, Der CJ. KRAS: The Critical Driver and Therapeutic Target for Pancreatic Cancer. Cold Spring Harb Perspect Med **2018**;8:a031435.
6. Bournet B, Muscari F, Buscail C, Assenat E, Barthet M, Hammel P*, et al.* KRAS G12D Mutation Subtype Is A Prognostic Factor for Advanced Pancreatic Adenocarcinoma. Clin Transl Gastroenterol **2016**;7:e157
7. Aguirre AJ, Bardeesy N, Sinha M, Lopez L, Tuveson DA, Horner J*, et al.* Activated Kras and Ink4a/Arf deficiency cooperate to produce metastatic pancreatic ductal adenocarcinoma. Genes Dev **2003**;17:3112-26
8. Collins MA, Bednar F, Zhang Y, Brisset JC, Galban S, Galban CJ*, et al.* Oncogenic Kras is required for both the initiation and maintenance of pancreatic cancer in mice. J Clin Invest **2012**;122:639-53
9. Guerra C, Schuhmacher AJ, Canamero M, Grippo PJ, Verdaguer L, Perez-Gallego L*, et al.* Chronic pancreatitis is essential for induction of pancreatic ductal adenocarcinoma by K-Ras oncogenes in adult mice. Cancer Cell **2007**;11:291-302
10. Hingorani SR, Petricoin EF, Maitra A, Rajapakse V, King C, Jacobetz MA*, et al.* Preinvasive and invasive ductal pancreatic cancer and its early detection in the mouse. Cancer Cell **2003**;4:437-50
11. Hingorani SR, Wang L, Multani AS, Combs C, Deramaudt TB, Hruban RH*, et al.* Trp53R172H and KrasG12D cooperate to promote chromosomal instability and widely metastatic pancreatic ductal adenocarcinoma in mice. Cancer Cell **2005**;7:469-83
12. Ying H, Kimmelman AC, Lyssiotis CA, Hua S, Chu GC, Fletcher-Sananikone E*, et al.* Oncogenic Kras maintains pancreatic tumors through regulation of anabolic glucose metabolism. Cell **2012**;149:656-70
13. Canon J, Rex K, Saiki AY, Mohr C, Cooke K, Bagal D*, et al.* The clinical KRAS(G12C) inhibitor AMG 510 drives anti-tumour immunity. Nature **2019**;575:217-23
14. Hallin J, Engstrom LD, Hargis L, Calinisan A, Aranda R, Briere DM*, et al.* The KRAS(G12C) Inhibitor MRTX849 Provides Insight toward Therapeutic Susceptibility of KRAS-Mutant Cancers in Mouse Models and Patients. Cancer Discov **2020**;10:54-71
15. Strickler JH, Satake H, George TJ, Yaeger R, Hollebecque A, Garrido-Laguna I*, et al.* Sotorasib in KRAS p.G12C-Mutated Advanced Pancreatic Cancer. N Engl J Med **2023**;388:33-43
16. Hallin J, Bowcut V, Calinisan A, Briere DM, Hargis L, Engstrom LD*, et al.* Anti-tumor efficacy of a potent and selective non-covalent KRAS(G12D) inhibitor. Nat Med **2022**;28:2171-82

17. Kemp SB, Cheng N, Markosyan N, Sor R, Kim IK, Hallin J, *et al.* Efficacy of a Small-Molecule Inhibitor of KrasG12D in Immunocompetent Models of Pancreatic Cancer. Cancer Discov **2023**;13:298-311
18. Hong DS, Fakih MG, Strickler JH, Desai J, Durm GA, Shapiro GI, *et al.* KRAS(G12C) Inhibition with Sotorasib in Advanced Solid Tumors. N Engl J Med **2020**;383:1207-17
19. Skoulidis F, Li BT, Dy GK, Price TJ, Falchook GS, Wolf J, *et al.* Sotorasib for Lung Cancers with KRAS p.G12C Mutation. N Engl J Med **2021**;384:2371-81
20. Awad MM, Liu S, Rybkin, II, Arbour KC, Dilly J, Zhu VW, *et al.* Acquired Resistance to KRAS(G12C) Inhibition in Cancer. N Engl J Med **2021**;384:2382-93
21. Collisson EA, Sadanandam A, Olson P, Gibb WJ, Truitt M, Gu S, *et al.* Subtypes of pancreatic ductal adenocarcinoma and their differing responses to therapy. Nat Med **2011**;17:500-3
22. Misale S, Fatherree JP, Cortez E, Li C, Bilton S, Timonina D, *et al.* KRAS G12C NSCLC Models Are Sensitive to Direct Targeting of KRAS in Combination with PI3K Inhibition. Clin Cancer Res **2019**;25:796-807
23. Ryan MB, Fece de la Cruz F, Phat S, Myers DT, Wong E, Shahzade HA, *et al.* Vertical Pathway Inhibition Overcomes Adaptive Feedback Resistance to KRAS(G12C) Inhibition. Clin Cancer Res **2020**;26:1633-43
24. Santana-Codina N, Chandhoke AS, Yu Q, Malachowska B, Kuljanin M, Gikandi A, *et al.* Defining and Targeting Adaptations to Oncogenic KRAS(G12C) Inhibition Using Quantitative Temporal Proteomics. Cell reports **2020**;30:4584-99 e4
25. Tu B, Yao J, Ferri-Borgogno S, Zhao J, Chen S, Wang Q, *et al.* YAP1 oncogene is a context-specific driver for pancreatic ductal adenocarcinoma. JCI Insight **2019;** 4:e130811
26. Zhao Y, Murciano-Goroff YR, Xue JY, Ang A, Lucas J, Mai TT, *et al.* Diverse alterations associated with resistance to KRAS(G12C) inhibition. Nature **2021**;599:679-83
27. Hou P, Kapoor A, Zhang Q, Li J, Wu CJ, Li J, *et al.* Tumor Microenvironment Remodeling Enables Bypass of Oncogenic KRAS Dependency in Pancreatic Cancer. Cancer Discov **2020**;10:1058-77
28. Hou P, Ma X, Yang Z, Zhang Q, Wu CJ, Li J, *et al.* USP21 deubiquitinase elevates macropinocytosis to enable oncogenic KRAS bypass in pancreatic cancer. Genes Dev **2021**;35:1327-32
29. Kapoor A, Yao W, Ying H, Hua S, Liewen A, Wang Q, *et al.* Yap1 activation enables bypass of oncogenic Kras addiction in pancreatic cancer. Cell **2014**;158:185-97
30. Barkal AA, Brewer RE, Markovic M, Kowarsky M, Barkal SA, Zaro BW, *et al.* CD24 signalling through macrophage Siglec-10 is a target for cancer immunotherapy. Nature **2019**;572:392-6
31. Bardeesy N, Aguirre AJ, Chu GC, Cheng KH, Lopez LV, Hezel AF, *et al.* Both p16(Ink4a) and the p19(Arf)-p53 pathway constrain progression of pancreatic adenocarcinoma in the mouse. Proc Natl Acad Sci U S A **2006**;103:5947-52
32. Zafra MP, Parsons MJ, Kim J, Alonso-Curbelo D, Goswami S, Schatoff EM, *et al.* An In Vivo Kras Allelic Series Reveals Distinct Phenotypes of Common Oncogenic Variants. Cancer Discov **2020**;10:1654-71

33. Kawaguchi Y, Cooper B, Gannon M, Ray M, MacDonald RJ, Wright CV. The role of the transcriptional regulator Ptf1a in converting intestinal to pancreatic progenitors. Nat Genet **2002**;32:128-34
34. Marino S, Vooijs M, van Der Gulden H, Jonkers J, Berns A. Induction of medulloblastomas in p53-null mutant mice by somatic inactivation of Rb in the external granular layer cells of the cerebellum. Genes Dev **2000**;14:994-1004
35. Bailey JM, Alsina J, Rasheed ZA, McAllister FM, Fu YY, Plentz R*, et al.* DCLK1 marks a morphologically distinct subpopulation of cells with stem cell properties in preinvasive pancreatic cancer. Gastroenterology **2014**;146:245-56
36. Storz P. Acinar cell plasticity and development of pancreatic ductal adenocarcinoma. Nat Rev Gastroenterol Hepatol **2017**;14:296-304
37. Ying H, Dey P, Yao W, Kimmelman AC, Draetta GF, Maitra A*, et al.* Genetics and biology of pancreatic ductal adenocarcinoma. Genes Dev **2016**;30:355-85
38. Leinwand J, Miller G. Regulation and modulation of antitumor immunity in pancreatic cancer. Nat Immunol **2020**;21:1152-9
39. Bailey P, Chang DK, Nones K, Johns AL, Patch AM, Gingras MC*, et al.* Genomic analyses identify molecular subtypes of pancreatic cancer. Nature **2016**;531:47-52
40. Hosein AN, Huang H, Wang Z, Parmar K, Du W, Huang J*, et al.* Cellular heterogeneity during mouse pancreatic ductal adenocarcinoma progression at single-cell resolution. JCI Insight **2019**;5:e129212
41. Elyada E, Bolisetty M, Laise P, Flynn WF, Courtois ET, Burkhart RA*, et al.* Cross-Species Single-Cell Analysis of Pancreatic Ductal Adenocarcinoma Reveals Antigen-Presenting Cancer-Associated Fibroblasts. Cancer Discov **2019;** 9:1102-1123.
42. Chen K, Wang Q, Li M, Guo H, Liu W, Wang F*, et al.* Single-cell RNA-seq reveals dynamic change in tumor microenvironment during pancreatic ductal adenocarcinoma malignant progression. EBioMedicine **2021**;66:103315
43. Eisenhauer EA, Therasse P, Bogaerts J, Schwartz LH, Sargent D, Ford R*, et al.* New response evaluation criteria in solid tumours: revised RECIST guideline (version 1.1). Eur J Cancer **2009**;45:228-47
44. Mahadevan KK, McAndrews KM, LeBleu VS, Yang S, Lyu H, Li B*, et al.* KRAS(G12D) inhibition reprograms the microenvironment of early and advanced pancreatic cancer to promote FAS-mediated killing by CD8(+) T cells. Cancer Cell **2023**
45. van Beek EM, Cochrane F, Barclay AN, van den Berg TK. Signal regulatory proteins in the immune system. J Immunol **2005**;175:7781-7
46. Majeti R, Chao MP, Alizadeh AA, Pang WW, Jaiswal S, Gibbs KD, Jr.*, et al.* CD47 is an adverse prognostic factor and therapeutic antibody target on human acute myeloid leukemia stem cells. Cell **2009**;138:286-99
47. Ihle JN. Cytokine receptor signalling. Nature **1995**;377:591-4
48. Hobbs GA, Baker NM, Miermont AM, Thurman RD, Pierobon M, Tran TH*, et al.* Atypical KRAS(G12R) Mutant Is Impaired in PI3K Signaling and Macropinocytosis in Pancreatic Cancer. Cancer Discov **2020**;10:104-23
49. Lee C, Jiang ZK, Planken S, Manzuk LK, Ortiz R, Hall M*, et al.* Efficacy and Imaging-Enabled Pharmacodynamic Profiling of KRAS G12C Inhibitors in Xenograft and Genetically Engineered Mouse Models of Cancer. Mol Cancer Ther **2023**;22:891-900
50. Arora N, Liang H, Zhou Y. RAS G-domains fine-tune the sorting of phosphatidylserine acyl chains in the plasma membrane. bioRxiv **2023**:2023.06.20.545612

51. Daniluk J, Liu Y, Deng D, Chu J, Huang H, Gaiser S, *et al.* An NF-kappaB pathway-mediated positive feedback loop amplifies Ras activity to pathological levels in mice. J Clin Invest **2012**;122:1519-28
52. Cook JH, Melloni GEM, Gulhan DC, Park PJ, Haigis KM. The origins and genetic interactions of KRAS mutations are allele- and tissue-specific. Nat Commun **2021**;12:1808
53. Mugarza E, van Maldegem F, Boumelha J, Moore C, Rana S, Llorian Sopena M, *et al.* Therapeutic KRAS(G12C) inhibition drives effective interferon-mediated antitumor immunity in immunogenic lung cancers. Sci Adv **2022**;8:eabm8780
54. Zhang X, Lan Y, Xu J, Quan F, Zhao E, Deng C, *et al*. CellMarker: a manually curated resource of cell markers in human and mouse. Nucleic Acids Res. **2019**; 47:D721-D728

Figure Legends

Figure 1. Tumor development is delayed in the $K^{C}PC$ model compared to $K^{D}PC$ model.

A. HE staining of mouse pancreas tissues from $K^{C}PC$ and $K^{D}PC$ model between 4 to 16 weeks. Scale bar: 50 μm. **B.** PanIN/ADM lesions numbers at different weeks of $K^{C}PC$ and $K^{D}PC$ mice under 200X fields. **C.** PanIN/ADM lesions area percentage at different weeks of $K^{C}PC$ and $K^{D}PC$ mice under 40X fields. **D. E,** Representative images and H score of p-ERK IHC staining of mice tissues at different weeks of $K^{C}PC$ and $K^{D}PC$ mice. Scale bar: 50 μm. **F. G**, Representative images and percentage of Ki67 IHC staining of mice tissues at different weeks of $K^{C}PC$ and $K^{D}PC$. Scale bar: 50 μm. **H.** Principle component analysis (PCA) of top 3000 variedly expressed genes showed a clear difference between G12D and G12C samples. **I.** Volcano plot of DEG analysis showed differentially expressed genes between G12D and G12C samples. Acinar cell marker genes (red) and progenitor cell marker genes (blue) are labelled. **J.** Gene set enrichment analysis (GSEA) plot showing the enrichment scores for acinar markers in G12C samples. **K.** GSEA plot showing the enrichment scores for exocrine progenitor markers in G12D samples. **L.** Multiplex immunofluorescent staining results showed composition of immune cell populations in different G12C and G12D samples. n.s. not significant. * $P<0.05$, *** $P<0.001$, ****$P<0.0001$

Figure 2. Advanced PDAC from $K^{C}PC$ and $K^{D}PC$ models exhibit similar histopathological and molecular features.

A, Kaplan–Meier curves depicting survival of $K^{C}PC$ and $K^{D}PC$ mice. Statistical significance was determined by the log-rank test. **B**, HE staining of mouse pancreas tumor tissues from $K^{C}PC$ and $K^{D}PC$ model. Scale bar: 50 μm. **C**, Representative images and H score of p-ERK IHC staining of mice tumor tissues of $K^{C}PC$ and $K^{D}PC$ model. Scale bar: 50 μm. n.s. not significant. **D**, Western

blots of whole-cell lysates from $K^{C}PC$ and $K^{D}PC$ cancer cell lines. **E**, PCA of top 5000 variedly expressed genes showed $K^{D}PC$ lines are clustered into two groups, and $K^{C}PC$ lines are clustered together with $K^{D}PC$ lines of the progenitor subtype. **F**, UMAP on three $K^{C}PC$ and $K^{D}PC$ tumor tissues. Populations are identified by color (see legend), Violin plots of key markers used to define the identified cell populations were shown in right panel. **G**, **H**, Integrated UMAP of cancer cells from $K^{C}PC$ and $K^{D}PC$ mice showing Louvain clusters (**G**) and tumor subtypes (**H**). **I, J**, Integrated UMAP of cancer-associated fibroblasts (CAFs) from $K^{C}PC$ and $K^{D}PC$ mice showing Louvain clusters (**I**) and CAF types (**J**).

Figure 3. $KRAS^{G12C}$ inhibitor reprograms PDAC tumor microenvironment and upregulates cancer cell CD24 expression.

A, B, Left, Growth curves of xenograft tumors (**A**,49725; **B**, 50760) show change in tumor volume over vehicle or AMG 510 treatment. Data, mean ± SEM. **Right**, Waterfall plot of vehicle- and AMG 510-treated tumors showing a change in tumor volume after treatment compared with baseline at day 0. Each bar represents a single tumor. **C,** Quantification of the immune cell populations by CyTOF immune profiling. Data, mean ± SEM; $n = 3$. The statistical difference between vehicle and AMG 510 treated groups was determined by two-tailed *t* tests. **D,** Quantification of macrophage populations by CyTOF analysis. Data, mean ± SEM; $n = 3$. **E**, Representative viSNE plots of p-SHP2+ macrophage populations in KRAS G12C mouse pancreatic tumor with vehicle or AMG 510 treatment. **F**, Quantification of p-SHP2+ macrophage populations in **E**. Data, mean ± SEM; $n = 3$. **G**, Median of membrane CD24+ in 50760 $K^{C}PC$ cancer cells treated with vehicle or AMG 510 was measured by flow cytometry. Data, mean ± SEM; the statistical difference between experimental groups was determined by two-tailed *t* tests. **H**, qRT-PCR for *CD24* expression in 50760 $K^{C}PC$ cancer cells treated with vehicle

or AMG 510. Data, mean ± SEM; $n = 3$. The statistical difference was determined by two-tailed *t* tests. **I**, Western blots of whole-cell lysates from vehicle or AMG 510 treated 50760 $K^{C}PC$ cancer cell lines. **J**, Median of membrane CD24+ in 50760 $K^{C}PC$ cancer cells treated with vehicle, AMG 510 or AMG plus C188-9 was measured by flow cytometry. Data, mean ± SEM; the statistical difference between experimental groups was determined by two-tailed *t* tests. **K**, qRT-PCR for *CD24* expression in 50760 $K^{C}PC$ cancer cells treated with vehicle, AMG 510 or AMG plus C188-9. Data, mean ± SEM; $n = 3$. The statistical difference was determined by two-tailed *t* tests. **L**, In vitro phagocytosis of mouse 50760-GFP PDAC cells cocultured with macrophage cell line RAW264.7 in the presence of AMG 510, anti-CD24 mAb, or dual treatment vs. IgG control. Phagocytosis was measured as the number of F4/80+, GFP+ macrophages, quantified as a percentage of the total F4/80+ macrophages. Data, mean ± SEM; n = 3. Statistics with significance were indicated n.s. not significant; * $P < 0.05$; ** $P < 0.01$; ***, $P < 0.001$, **** $P < 0.0001$.

Figure 4. Targeting CD24 sensitizes pancreatic cancer to both $KRAS^{G12C}$ *and* $KRAS^{G12D}$ inhibitors in vivo.

A, B, Top, Growth curves of xenograft $K^{C}PC$ tumors (**A**,49725; **B**, 50760) show change in tumor volume over vehicle, anti-CD24, AMG 510 or anti-CD24 + AMG 510 treatment. Data, mean ± SEM. **Bottom**, Waterfall plot of vehicle-, anti-CD24-, AMG 510- or anti-CD24 + AMG 510-treated tumors showing a change in tumor volume after treatment compared with baseline at day 0. Each bar represents a single tumor. **C**, In vivo phagocytosis. Mouse 50760-GFP PDAC cells were injected into the right flank of C57BL/6 mice and treated with IgG control or AMG 510+ anti-CD24 mAb for 14 days. Mice tumor tissues were collected for flow cytometry. Phagocytosis was measured as the number of F4/80+, GFP+ macrophages, quantified as a

percentage of the total F4/80+ macrophages. Data, mean ± SEM; $n = 4$. **D**, Mice tumor tissues collected in **C** were measured by flow cytometry for F4/80 and p-SHP2. Percentage of p-SHP2+ macrophages were compared in IgG control or AMG 510+ anti-CD24 mAb groups. Data, mean ± SEM; n = 4. **E**, Growth curves of xenograft $K^{C}PC$ tumor (49725) show changes in tumor volume over vehicle, vehicle + anti-CSF1R, anti-CD24 + AMG 510 (combination), or anti-CSF1R + combination treatment. Data, mean ± SEM. **F**, Median of membrane CD24+ in $K^{D}PC$ cancer cells (55582) treated with vehicle or MRTX1133 was measured by flow cytometry. Data, mean ± SEM; the statistical difference between experimental groups was determined by two-tailed *t* tests. **G**, qRT-PCR for *CD24* expression in $K^{D}PC$ cancer cells (55582) treated with vehicle or MRTX1133. Data, mean ± SEM; $n = 3$. The statistical difference was determined by two-tailed *t* tests. **H**, **Left**, Growth curves of xenograft $K^{D}PC$ tumor (55582) show change in tumor volume over vehicle, anti-CD24, MRTX1133 or anti-CD24 + MRTX1133 treatment. Data, mean ± SEM. **Right**, Waterfall plot of vehicle, anti-CD24, MRTX1133 or anti-CD24 + MRTX1133-treated tumors showing a change in tumor volume after treatment compared with baseline at day 0. Each bar represents a single tumor. **I**, **Top**, Growth curves of human KRAS G12D tumors (AsPC1) show change in tumor volume over vehicle, anti-CD24, MRTX1133 or anti-CD24 + MRTX1133 treatment. Data, mean ± SEM. **Bottom,** Waterfall plot of vehicle, anti-CD24, MRTX1133 or anti-CD24 + MRTX1133-treated tumors showing a change in tumor volume after treatment compared with baseline at day 0. Each bar represents a single tumor. Statistics with significance were indicated n.s. not significant; * $P < 0.05$; ** $P < 0.01$; ***, $P < 0.001$, **** $P < 0.0001$.

Supplementary Figure S1.

A, AOIs selections for GeoMx digital spatial profiler RNA profiling analysis of $K^{C}PC$ and $K^{D}PC$ PanIN lesions. FFPE sections were imaged using three-color fluorescence of PanCK, CD45, and DNA to establish overall tissue morphology. For each section, 13-20 AOIs of 200 µm in diameter were selected base on PanCK+ expression for detailed molecular profiling with RNA probe cocktail. Scale bar, 500 µm. **B,** GSEA term heatmap showed acinar markers are up in G12C samples. **C,** GSEA term heatmap showed exocrine progenitor markers are up in G12D samples. **D,** Representative images of CK19 IHC staining of mice pancreas tissues at 16 weeks of age of $K^{C}PC$ and $K^{D}PC$. Scale bar: 50 µm. **E**, Immunofluorescent staining of CK19 and amylase in mice pancreas tissues at 16 weeks of age of $K^{C}PC$ and $K^{D}PC$. Nuclei were counterstained with DAPI. Scale bar: 10 µm. **F**, Immunofluorescent staining of CK19 and DCLK1 in mice pancreas tissues at 16 weeks of age of $K^{C}PC$ and $K^{D}PC$. Nuclei were counterstained with DAPI. Scale bar: 10 µm. **G.** Representative multiplex immunofluorescent staining images in mice pancreas tissues at 16 weeks of age of $K^{C}PC$ and $K^{D}PC$. Scale bar: 100 µm.

Supplementary Figure S2.

A, Kaplan–Meier curves depicting overall survival of 231 PDAC patients. Statistical significance was determined by the log-rank test. **B**, Western blots of whole-cell lysates from $K^{C}PC$ and $K^{D}PC$ cancer cell lines. **C**, Violin plots of key markers used to define the identified cancer cell populations. **D**, Violin plots of key markers used to define the identified CAF cell populations.

Supplementary Figure S3.

A, IC_{50} values for AMG 510 in two mice KRAS G12C cell lines was determined by MTT assay. **B**, CyTOF immune profiling by viSNE of KRAS G12C mouse pancreatic tumors with vehicle or

AMG 510 treatment. **C**, Representative viSNE plots of macrophage populations in KRAS G12C mouse pancreatic tumor with vehicle or AMG 510 treatment. **D,** IHC of xenograft tumors showing phosphor-ERK was reduced whereas $CD8^+$ T cells and $F4/80^+$ macrophages were increased in AMG 510-treated tumors compared to vehicle-treated group. **E,** CyTOF analysis demonstrates that CD24 intensity was upregulated in cancer cells after AMG 510 treatment. **Left**, quantification of CD24 intensity. **Right**, representative viSNE plots of CD24 staining in tumors with vehicle or AMG 510 treatment. Data, mean ± SEM; $n = 3$. **F,** Median of membrane CD24+ in 49725 K^CPC cancer cells treated with vehicle or AMG 510 was measured by flow cytometry. Data, mean ± SEM. **G,** Median of membrane CD24+ (top) or CD47+ (bottom) in 50760 K^CPC cancer cells treated with vehicle or AMG 510 was measured by flow cytometry. Data, mean ± SEM. **H,** Kinase array analysis indicated that AMG 510 treatment in 50760 K^CPC cancer cells results in decrease of p-ERK and p-c-Jun and increase of p-STAT3 (Y705). **I,** Western blots of whole-cell lysates from vehicle, AMG 510 or AMG 510 plus C188-9 treated 50760 K^CPC cancer cell lines.

Supplementary Figure S4A

Macrophage depletion by anti-CSF1R antibody. Mice received 400 μg of anti-CSF1R antibody i.p., every other day whereas control mice were given isotype IgG control. Tumor tissues were collected to confirm macrophage depletion via flow cytometry. Data shown both PE-F4/80+ and PerCP5.5-CD45+ macrophages were 0.25% in CSF1R treated group, compared to 4.72% in IgG treated group.

Acknowledgments

This study was funded by NIH R01CA214793 and The MD Anderson Cancer Center SPORE in Gastrointestinal Cancer DRP Grant P50 CA221707 (to H. Ying), NIH P01CA117969 (to H. Ying, H. Wang, and R.A. Depinho), NIH 1R01CA272744 and ACS RSG-22-017-01-CCB (to W.Yao), The MD Anderson Cancer Center SPORE in Gastrointestinal Cancer CEP Grant P50 CA221707 (to Y. Wei), CPRIT Training Award RP210028 (to E. Y. Yen) and The MD Anderson Cancer Center Support Grant NIH P30 CA016672. We acknowledge The MD Anderson Cancer Center Flow Cytometry and Cellular Imaging Core Facility, Research Histology Core Laboratory and Advanced Technology Genomics Core (ATGC). We thank Dr. Anirban Maitra for the insightful suggestions during the execution of the experiments and writing of manuscript. We are thankful to members of the Ying and Yao laboratories for their comments and suggestions.

Authors' Contributions

Y. Wei: Conceptualization, formal analysis, validation, investigation, visualization, methodology, writing–original draft, writing–review and editing. **M. Liu:** Formal analysis, validation and investigation. **E. Y. Yen:** Formal analysis, methodology, validation and investigation. **J. Yao:** Formal analysis, methodology, validation and investigation. **P.T. Nguyen:** Formal analysis, validation and investigation. **X. Wang:** Methodology, validation and investigation. **Z. Yang:** Validation and investigation. **A. Yousef:** Validation and investigation. **D. Pan:** Methodology, validation and investigation. **Y. Jin:** Methodology, validation and investigation. **M.S. Theady:** Validation and investigation. **J. Park:** Validation and investigation. **Y. Cai:** Validation and investigation. **M. Takeda:** Validation and investigation. **M. Vasquez:** Formal analysis, methodology and investigation. **Y. Zhou:** Validation and investigation. **H.**

Zhao: Supervision and investigation. **A. Viale:** Supervision and investigation. **H. Wang:** Supervision, resources and investigation. **D. Zhao:** Resources and investigation. **R.A. DePinho:** Supervision, resources, visualization, writing–review and editing. **W. Yao:** Conceptualization, resources, formal analysis, supervision, funding acquisition, validation, investigation, visualization, methodology, writing–original draft, project administration, writing–review and editing. **H. Ying:** Conceptualization, resources, formal analysis, supervision, funding acquisition, validation, investigation, visualization, methodology, writing–original draft, project administration, writing–review and editing.

Supplementary Table S1 Percentage of different cell types in mouse KRAS G12C and G12D tumor tissues

Annotation	G12C_6304	G12C_7825	G12C_9726	G12D_4956	G12D_57614	GSM3577885
Neutrophil	40.46%	70.59%	9.92%	9.71%	20.00%	13.29%
Tumor	17.16%	5.99%	40.82%	33.48%	43.06%	16.85%
iCAF	14.59%	0.96%	16.62%	29.83%	21.73%	6.64%
Macrophage	8.98%	8.43%	1.06%	5.82%	4.28%	45.63%
B	3.60%	4.89%	9.48%	5.71%	5.61%	10.84%
T	3.80%	7.23%	9.60%	0.80%	2.45%	1.64%
Endothelial	8.37%	0.33%	3.06%	8.11%	0.41%	0.17%
Proliferative	1.18%	1.40%	1.58%	1.26%	1.73%	4.51%
myCAF	1.16%	0.17%	3.94%	5.14%	0.71%	0.03%
Acinar	0.68%	0.00%	3.92%	0.11%	0.00%	0.38%

Supplementary Table S2. Percentage of immune cells in mouse KRAS G12C and G12D tumors tissues

Annotation	G12C_6304	G12C_7825	G12C_9726	G12D_4956	G12D_57614	GSM3577885
B	4.73%	3.81%	36.30%	8.11%	14.55%	1.26%
DC	9.03%	3.88%	3.21%	21.08%	3.94%	28.46%
Macrophage	2.09%	1.12%	1.07%	1.08%	2.12%	36.83%
Monocyte	5.98%	5.99%	2.80%	21.62%	8.79%	19.45%
Neutrophil	71.06%	78.28%	20.00%	44.32%	60.61%	11.34%
Plasma	0.67%	0.25%	2.14%	0%	3.03%	0.35%
T	6.44%	6.68%	34.49%	3.78%	6.97%	2.32%

Supplementary Table S3 Antibodies list

Flow cytometry antibodies

Antibody	Supplier	Clone	Cat#	Dilution
Phospho-Shp2 (Tyr580) PE	ThermoFisher	Shp2Y580-4A2	MA5-36978	1:100
F4/80 PerCP	Biolegend	BM8	123125	1:100
F4/80 PE	Biolegend	BM8	123110	1:100
CD47 PE	Biolegend	miap301	127507	1:100
CD24 PE	Biolegend	M1/69	101807	1:100
CD45 PerCP/Cy5.5	Biolegend	30-F11	103131	1:100

Immunostaining and immunoblotting antibodies

Antibody	Supplier	Cat#
CK19	Proteintech	14965-I-AP
CD8a	Cell Signaling	98941
Ki67	Abcam	Ab15580
F4/80	Cell Signaling	70076
P-AKT (S473)	Cell Signaling	4051
P-STAT3 (Y705)	Cell Signaling	9145
P-ERK1/2	Cell Signaling	9101
DCLK1	Cell Signaling	62257

Multiplex immunofluorescent staing antibodies

Target	Supplier	Cat#
B220, CD45R	BD	553084
Ly-6G	BD	551459
CD11c	Cell Signaling	97585S
CD4	Thermo Fisher	14-9766-80
CD45	Abcam	ab10558
PD-L1/CD274	Proteintech	66248-1-Ig
Arginase1	Abcam	ab91279
iNos	Cell Signaling	13120S
CD3e 594	Agilent Technologies	A045229-2
Foxp3 647	Cell Signaling	12653S
CD8 594	Thermo Fisher	14-0808-80
F4/80	Cell Signaling	70076S
Granzyme B	Thermo Fisher	14-8822-80
Amylase	Santa cruz	sc-46657
CD11b	Abcam	ab133357

CyTOF antibodies

Tagged Abs. description	Target	label	Clone	Source	Cat#
CD45(Ms) 89Y	CD45(Ms)	89Y	30-F11	DVS-Fluidigm	3089005B
CD4(Ms) 115In	CD4(Ms)	115In	RM4-5	BioLegend	100506
CD8a(Ms) 146Nd (MDA)	CD8a	146Nd	53-6.7	BioLegend	100702
CD44 160Gd	CD44	160Gd	IM7	BioLegend	103002
CD62L(Ms) 155Gd	CD62L	155Gd	MEL-14	BioLegend	104402
Granzyme B 173Yb	Granzyme B	173Yb	GB11	DVS-Fluidigm	3173006B
IFNg(Ms) 165Ho	IFNg	165Ho	XMG1.2	DVS-Fluidigm	3165003B
CD11b 148Nd	CD11b	148Nd	M1/70	DVS-Fluidigm	3148003B
CD11c(Ms) 142Nd (MDA)	CD11c	142Nd	N418	BioLegend	117302
CD19(Ms) 149Sm (MDA)	CD19	149Sm	4D5	BioLegend	115502
CD274(Ms) 154Sm	CD274, PD-L1	154Sm	10F.9G2	BioLegend	124303
CD3e 152Sm (MDA)	CD3, CD3e	152Sm	145-2C11	BioLegend	100302
Foxp3(Ms) 158Gd	Foxp3	158Gd	FJK-16s	DVS-Fluidigm	3158003A
I-A/I-E 209Bi	I-A/I-E, MHC-II	209Bi	M5/114.15.2	DVS-Fluidigm	3209006B
F4/80(Ms) 159Tb (MDA)	F4/80	159Tb	BM8	BioLegend	123102
TIGIT(Ms) 151Eu	TIGiT, Vstm3	151Eu	1G9	BioLegend	142102
TIM-3(Ms) 162Dy	TIM3, CD366	162Dy	RMT3-23	DVS-Fluidigm	3162029B
CD80(Ms) 171Yb	CD80	171Yb	16-10A10	DVS-Fluidigm	3171008B
Arginase-1 153Eu	Arginase 1	153Eu	Polyclonal	R&D	AF5868
CD152(Ms) 163Dy	CD152, CTLA-4	163Dy	9H10	BioLegend	106202
Ki67 168Er	Ki67	168Er	B56	BD	556003
NK1.1(Ms) 170Er	NK1.1, CD161b/c, Ly-55	170Er	PK136	DVS-Fluidigm	3170002B
CD24(Ms) 169Tm	CD24	169Tm	M1/69	BioLegend	101802
H3K27me2me3 139La	Histone H3K27me2me3	139La	Ascites	ActiveMotif	39535
iNOS(Ms) 161Dy	iNOS	161Dy	CXNFT	DVS-Fluidigm	3161011B
CD25(Ms) 167Er	CD25	167Er	PC61.5	Tonbo	70-0251-U100
CD279(Ms) 150Nd (RMP1-30)	CD279, PD-1	150Nd	RMP1-30	Tonbo	70-9981-U500
Ly-6G/C 175Lu	Ly-6G/Ly-6C, Gr-1	175Lu	RB6-8C5	BioLegend	108402
CD223(Ms) 147Sm	CD223, LAG-3	147Sm	C9B7W	BioLegend	125202

CD49b(Ms) 164Dy	CD49b	164Dy	HMa2	DVS-Fluidigm	3164011B
p-SHP2 141Pr	p-SHP2	141Pr	D66F10	DVS-Fluidigm	3141002A
NKG2A(Ms) 166Er	NKG2A, CD159a	166Er	70589	R&D	MAB6867

Figure 1

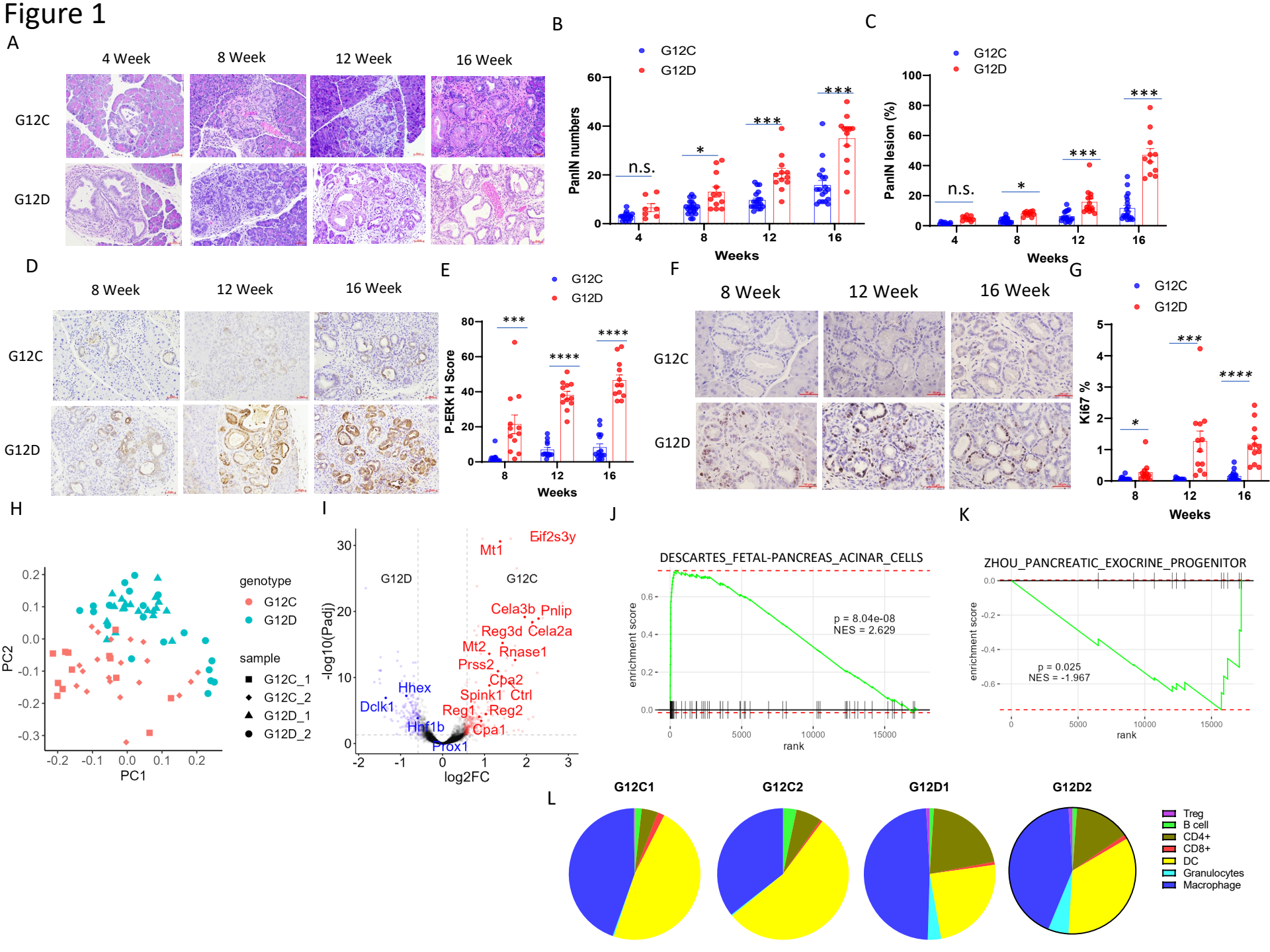
A
4 Week
8 Week
12 Week
16 Week
G12C
G12D
B
PanIN numbers
Weeks
n.s.
*
***
***
C
PanIN lesion (%)
Weeks
n.s.
*
***
***
D
8 Week
12 Week
16 Week
E
P-ERK H Score
Weeks
***
****
****
F
8 Week
12 Week
16 Week
G
Ki67 %
Weeks
*
***
****
H
PC2
PC1
genotype
G12C
G12D
sample
G12C_1
G12C_2
G12D_1
G12D_2
I
-log10(Padj)
log2FC
G12D
G12C
Eif2s3y
Mt1
Cela3b
Pnlip
Reg3d
Cela2a
Mt2
Rnase1
Prss2
Cpa2
Spink1
Ctrl
Reg1
Reg2
Cpa1
Hhex
Dclk1
Hnf1b
Prox1
J
DESCARTES_FETAL-PANCREAS_ACINAR_CELLS
enrichment score
rank
p = 8.04e-08
NES = 2.629
K
ZHOU_PANCREATIC_EXOCRINE_PROGENITOR
enrichment score
rank
p = 0.025
NES = -1.967
L
G12C1
G12C2
G12D1
G12D2
Treg
B cell
CD4+
CD8+
DC
Granulocytes
Macrophage

Figure 2

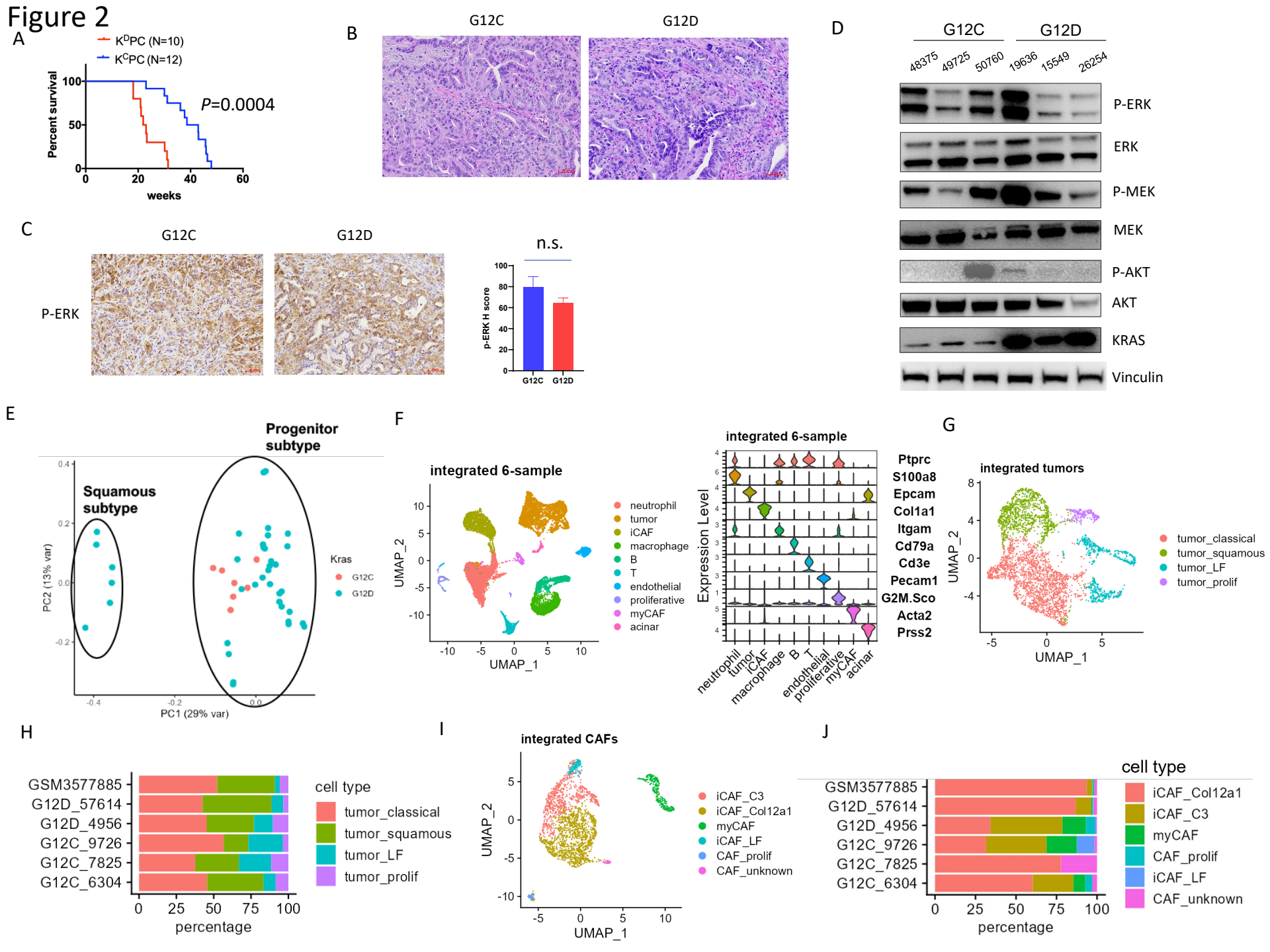
A
K^DPC (N=10)
K^CPC (N=12)
Percent survival
P=0.0004
weeks
B
G12C
G12D
C
G12C
G12D
P-ERK
n.s.
p-ERK H score
G12C
G12D
D
G12C
G12D
48375
49725
50760
19636
15549
26254
P-ERK
ERK
P-MEK
MEK
P-AKT
AKT
KRAS
Vinculin
E
Progenitor subtype
Squamous subtype
PC2 (13% var)
PC1 (29% var)
Kras
G12C
G12D
F
integrated 6-sample
UMAP_2
UMAP_1
neutrophil
tumor
iCAF
macrophage
B
T
endothelial
proliferative
myCAF
acinar
integrated 6-sample
Expression Level
Ptprc
S100a8
Epcam
Col1a1
Itgam
Cd79a
Cd3e
Pecam1
G2M.Sco
Acta2
Prss2
G
integrated tumors
UMAP_2
UMAP_1
tumor_classical
tumor_squamous
tumor_LF
tumor_prolif
H
GSM3577885
G12D_57614
G12D_4956
G12C_9726
G12C_7825
G12C_6304
percentage
cell type
tumor_classical
tumor_squamous
tumor_LF
tumor_prolif
I
integrated CAFs
UMAP_2
UMAP_1
iCAF_C3
iCAF_Col12a1
myCAF
iCAF_LF
CAF_prolif
CAF_unknown
J
GSM3577885
G12D_57614
G12D_4956
G12C_9726
G12C_7825
G12C_6304
percentage
cell type
iCAF_Col12a1
iCAF_C3
myCAF
CAF_prolif
iCAF_LF
CAF_unknown

Figure 3

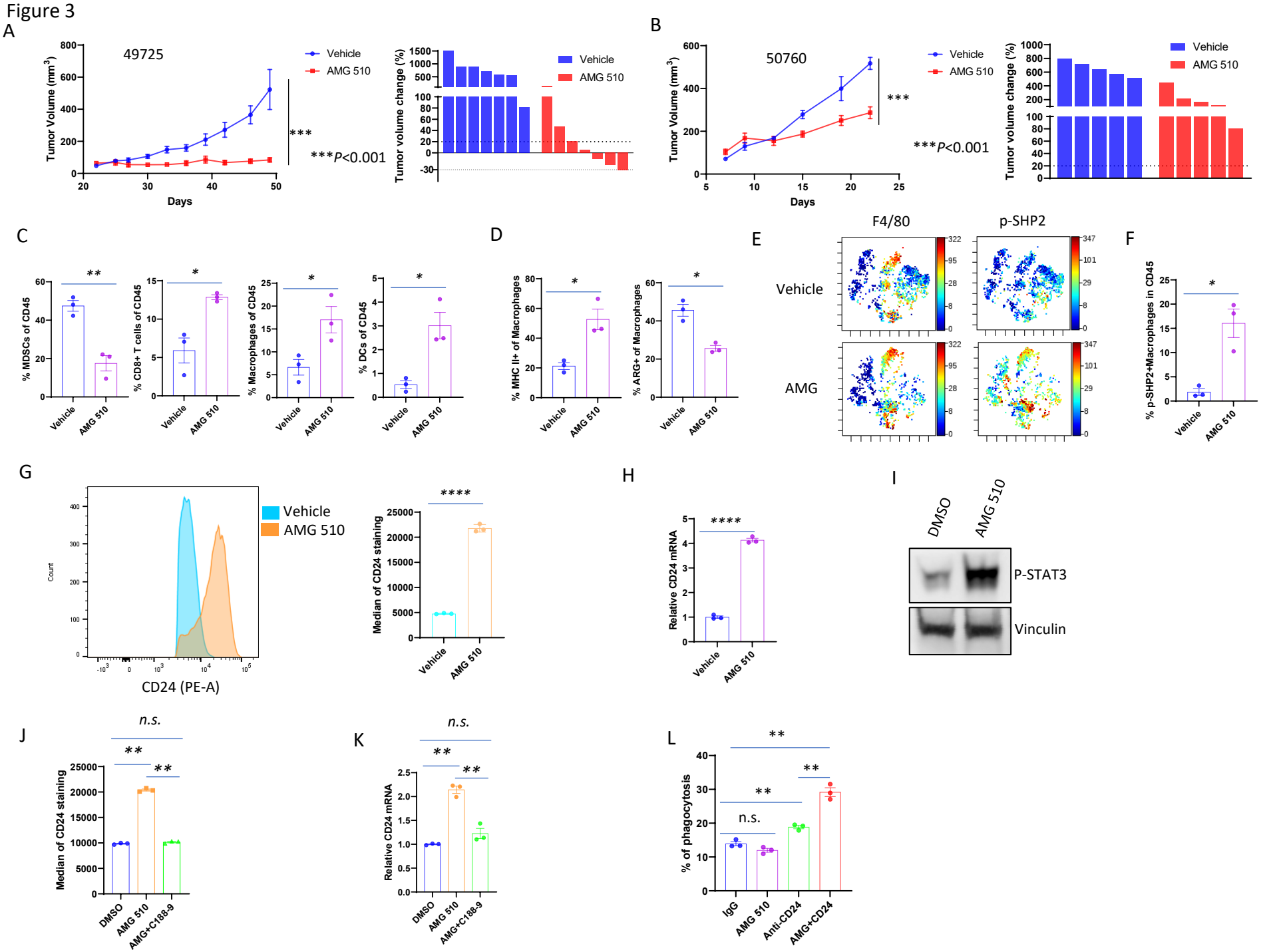
A
49725
Vehicle
AMG 510
Tumor Volume (mm³)
Days
***
***P<0.001
Tumor volume change (%)
B
50760
***P<0.001
C
% MDSCs of CD45
% CD8+ T cells of CD45
% Macrophages of CD45
% DCs of CD45
D
% MHC II+ of Macrophages
% ARG+ of Macrophages
E
F4/80
p-SHP2
Vehicle
AMG
F
% p-SHP2+Macrophages in CD45
G
Count
CD24 (PE-A)
Median of CD24 staining
H
Relative CD24 mRNA
I
DMSO
AMG 510
P-STAT3
Vinculin
J
n.s.
Median of CD24 staining
DMSO
AMG+C188-9
K
Relative CD24 mRNA
L
% of phagocytosis
IgG
Anti-CD24
AMG+CD24

Figure 4

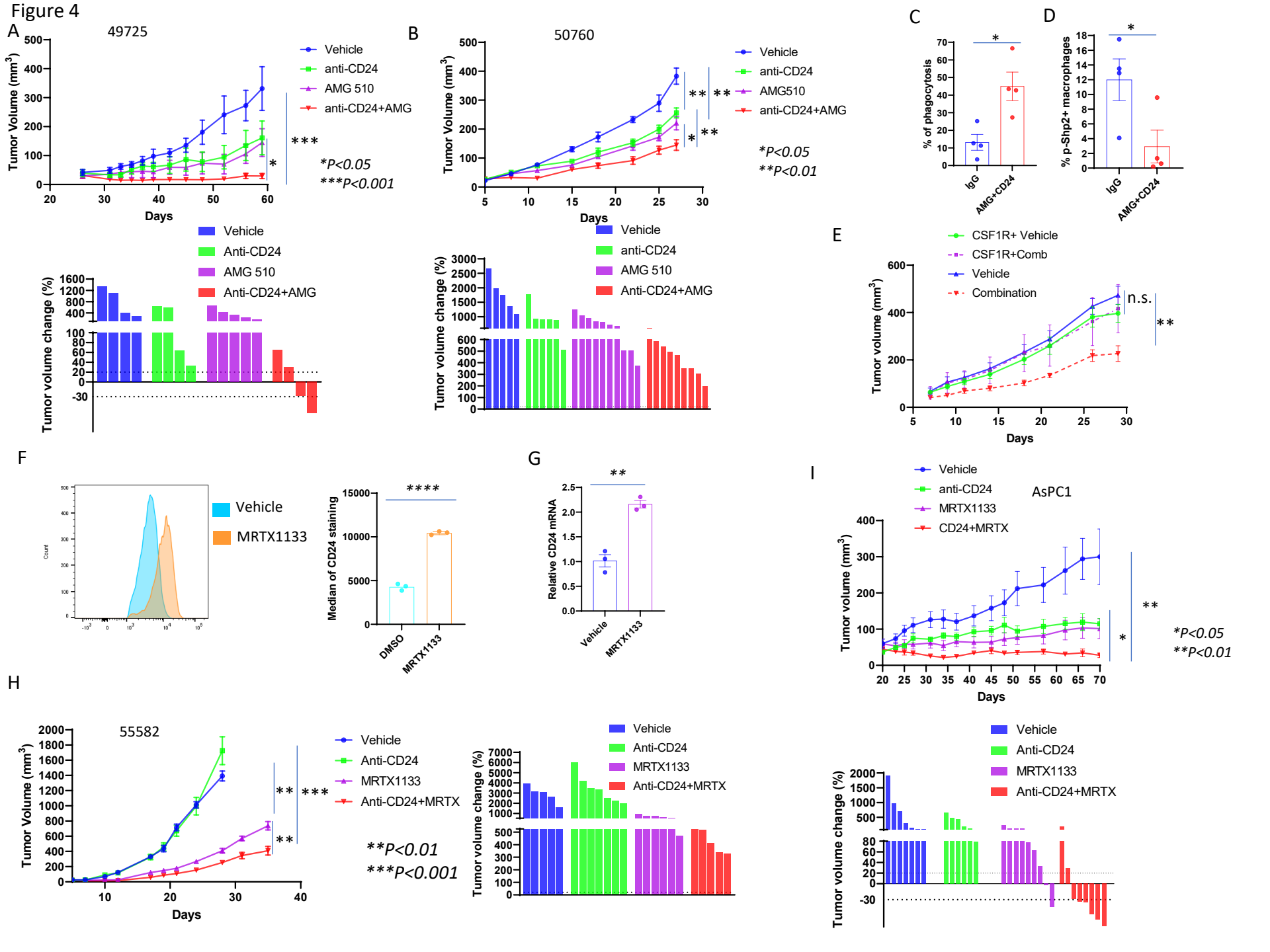
A
49725
Tumor Volume (mm3)
Days
Vehicle
anti-CD24
AMG 510
anti-CD24+AMG
*P<0.05
***P<0.001
Tumor volume change (%)
Anti-CD24
Anti-CD24+AMG
B
50760
AMG510
*P<0.05
**P<0.01
C
% of phagocytosis
IgG
AMG+CD24
D
% p-Shp2+ macrophages
E
CSF1R+ Vehicle
CSF1R+Comb
Combination
Tumor volume (mm3)
n.s.
F
Count
MRTX1133
Median of CD24 staining
DMSO
G
Relative CD24 mRNA
I
AsPC1
CD24+MRTX
H
55582
Anti-CD24+MRTX
**P<0.01
***P<0.001

Supplementary Fig. S1

A

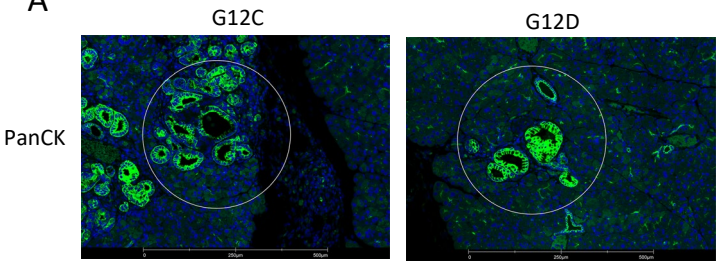

B

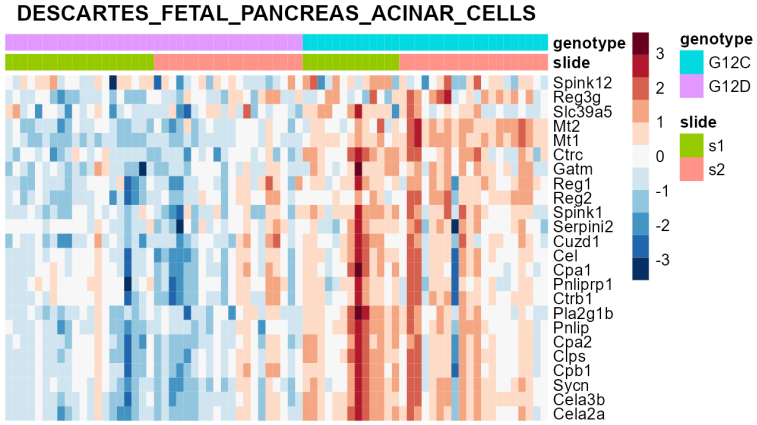

C

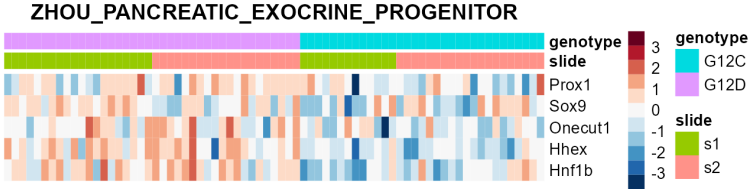

D

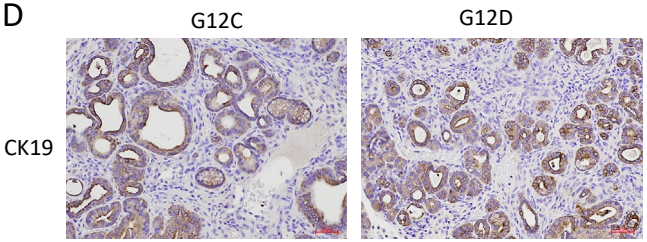

E

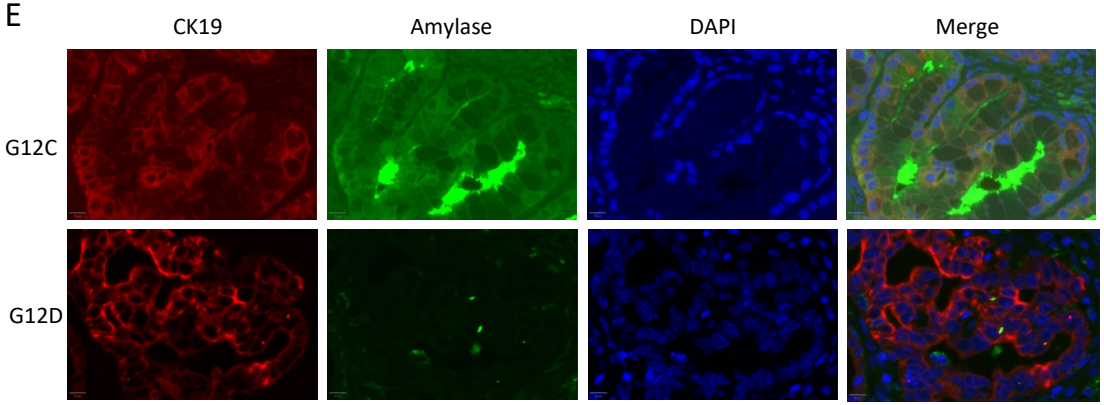

F

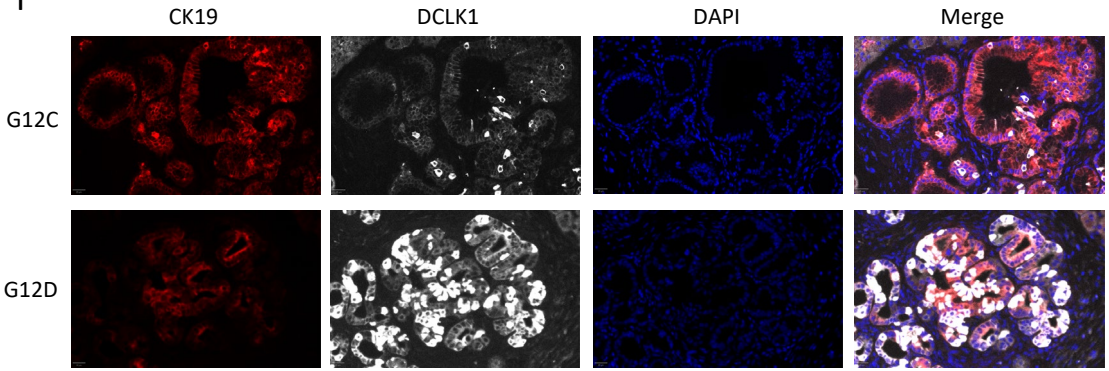

G

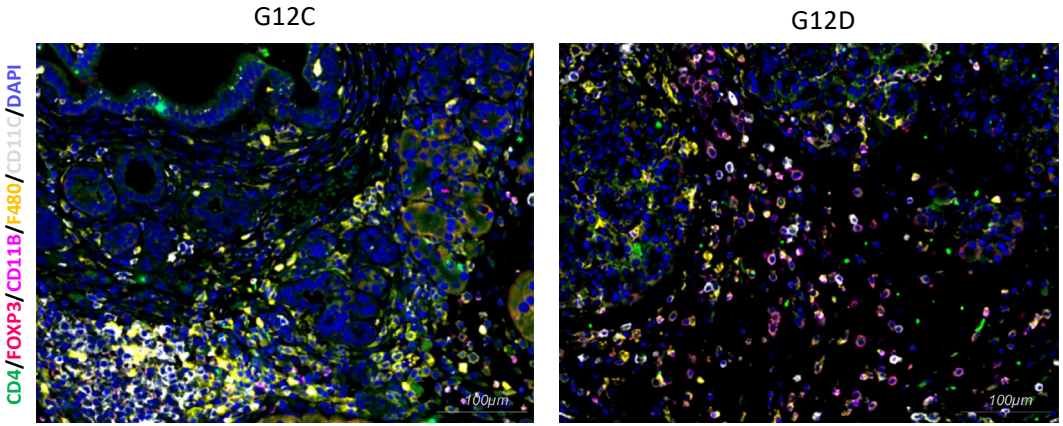

Supplementary Fig. S2

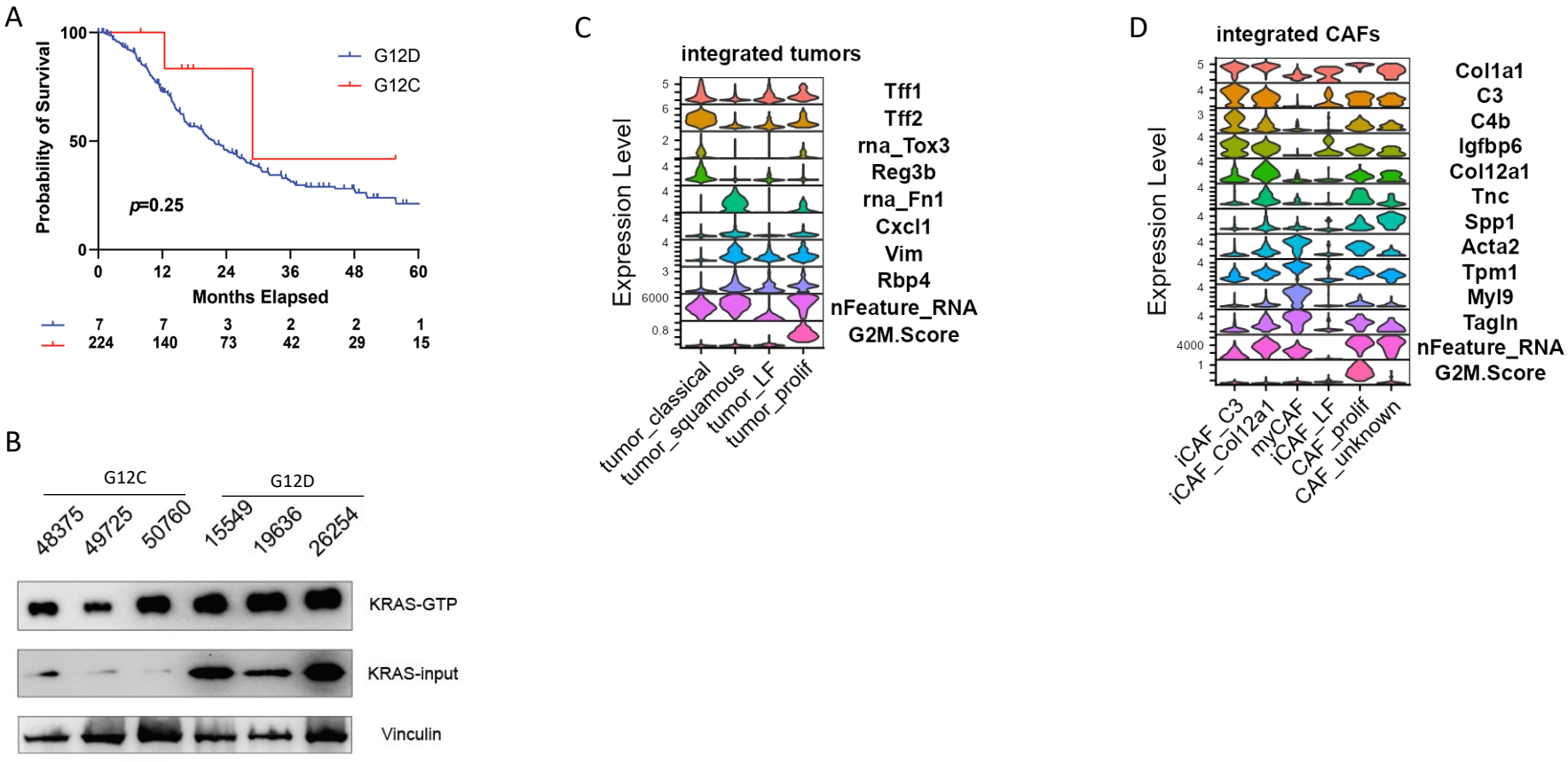

Supplementary Fig. S3

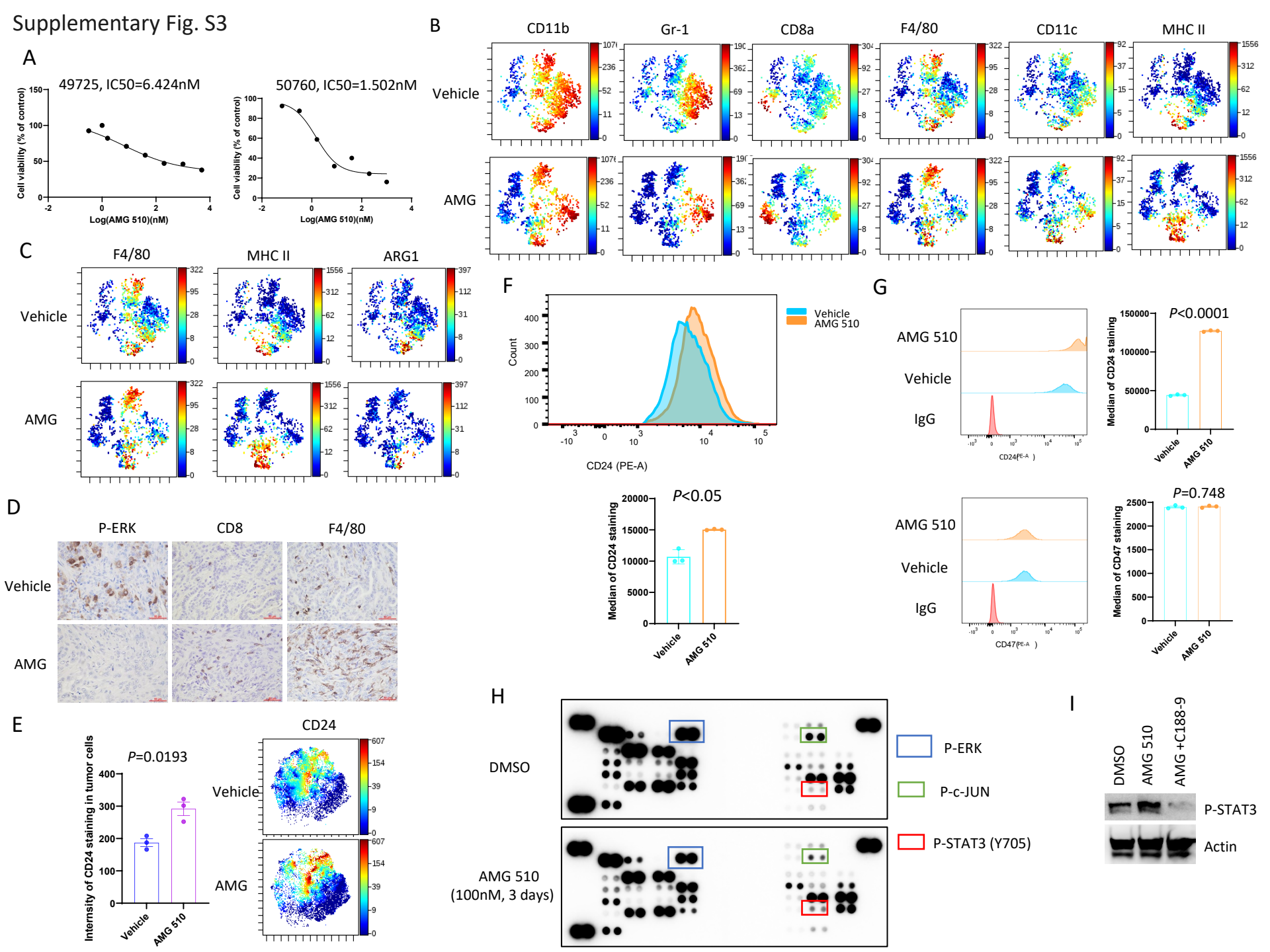
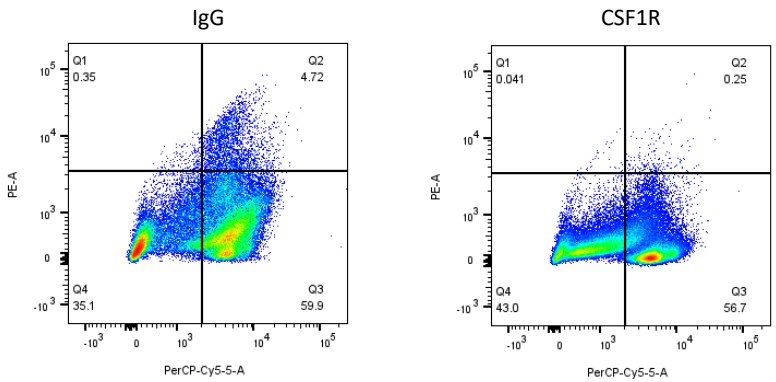
Supplementary Fig. S4A